

Special Section:

Land-atmosphere coupling:
measurement, modelling and
analysis

Key Points:

- The scale-dependent distribution of latent heat flux, vertical velocity variance, and water vapor variance at 100 m over a heterogeneous surface is described
- In the large-eddy scale, 70% of total latent heat flux is contributed by 50% of total vertical velocity variance and 50% of total water vapor variance
- The large-eddy scale contributes most of the vertical moisture transport from the surface to the Planetary Boundary Layer

Correspondence to:

Z. Wang,
Zhien.Wang@stonybrook.edu

Citation:

Lin, G., Wang, Z., Chu, Y., Ziegler, C. L., Hu, X.-M., Xue, M., et al. (2024). Airborne measurements of scale-dependent latent heat flux impacted by water vapor and vertical velocity over heterogeneous land surfaces during the CHEESEHEAD19 campaign. *Journal of Geophysical Research: Atmospheres*, 129, e2023JD039586. <https://doi.org/10.1029/2023JD039586>

Received 3 JUL 2023

Accepted 17 JAN 2024

Author Contributions:

Conceptualization: Guo Lin, Zhien Wang

Data curation: Zhien Wang, Ankur R. Desai, Min Deng

Formal analysis: Guo Lin, Zhien Wang, Yufei Chu, Xiao-Ming Hu, Ming Xue, Bart Geerts, Ankur R. Desai

Funding acquisition: Zhien Wang, Ankur R. Desai

© 2024 The Authors.

This is an open access article under the terms of the Creative Commons Attribution-NonCommercial License, which permits use, distribution and reproduction in any medium, provided the original work is properly cited and is not used for commercial purposes.

Airborne Measurements of Scale-Dependent Latent Heat Flux Impacted by Water Vapor and Vertical Velocity Over Heterogeneous Land Surfaces During the CHEESEHEAD19 Campaign

Guo Lin^{1,2} , Zhien Wang³, Yufei Chu³, Conrad L. Ziegler^{4,5}, Xiao-Ming Hu^{5,6} , Ming Xue^{5,6} , Bart Geerts⁷ , Sreenath Paleri⁸ , Ankur R. Desai⁸ , Kang Yang³ , Min Deng⁹, and Jonathan DeGraw^{5,6}

¹NOAA/AOML/Hurricane Research Division, Miami, FL, USA, ²Cooperative Institute for Marine and Atmospheric Studies, University of Miami, Miami, FL, USA, ³School of Marine and Atmospheric Sciences, Stony Brook University, Stony Brook, NY, USA, ⁴NOAA/National Severe Storms Laboratory, Norman, OK, USA, ⁵School of Meteorology, University of Oklahoma, Norman, OK, USA, ⁶Center for Analysis and Prediction of Storms, University of Oklahoma, Norman, OK, USA, ⁷Department of Atmospheric Science, University of Wyoming, Laramie, WY, USA, ⁸Department of Atmospheric and Oceanic Sciences, University of Wisconsin-Madison, Madison, WI, USA, ⁹Environmental and Climate Sciences Department, Brookhaven National Laboratory, Upton, NY, USA

Abstract The water vapor transport associated with latent heat flux (LE) in the planetary boundary layer (PBL) is critical for the atmospheric hydrological cycle, radiation balance, and cloud formation. The spatiotemporal variability of LE and water vapor mixing ratio (r_v) are poorly understood due to the scale-dependent and nonlinear atmospheric transport responses to land surface heterogeneity. Here, airborne in situ measurements with the wavelet technique are utilized to investigate scale-dependent relationships among LE, vertical velocity (w) variance (σ_w^2), and r_v variance (σ_{H2O}^2) over a heterogeneous surface during the Chequamegon Heterogeneous Ecosystem Energy-balance Study Enabled by a High-density Extensive Array of Detectors 2019 (CHEESEHEAD19) field campaign. Our findings reveal distinct scale distributions of LE, σ_w^2 , and σ_{H2O}^2 at 100 m height, with a majority scale range of 120 m–4 km in LE, 32 m–2 km in σ_w^2 , and 200 m–8 km in σ_{H2O}^2 . The scales are classified into three scale ranges, the turbulent scale (8–200 m), large-eddy scale (200 m–2 km), and mesoscale (2–8 km) to evaluate scale-resolved LE contributed by σ_w^2 and σ_{H2O}^2 . The large-eddy scale in PBL contributes over 70% of the monthly mean total LE with equal parts (50%) of contributions from σ_w^2 and σ_{H2O}^2 . The monthly temporal variations mainly come from the first two major contributing classified scales in LE, σ_w^2 , and σ_{H2O}^2 . These results confirm the dominant role of the large-eddy scale in the PBL in the vertical moisture transport from the surface to the PBL, while the mesoscale is shown to contribute an additional ~20%. This analysis complements published scale-dependent LE variations, which lack detailed scale-dependent vertical velocity and moisture information.

Plain Language Summary The vertical water vapor transport in the planetary boundary layer (PBL), and the associated latent heat flux (LE), are critical for the atmospheric hydrological cycle, radiation balance, and cloud formation. However, the vertical moisture transport varies nonlinearly at multiple scales due to the land surface heterogeneity across multiple properties. This study investigates the scale-resolved impact of water vapor and vertical velocity on LE, using data collected aboard an atmospheric research aircraft flying low above the surface in summer over northern Wisconsin during the CHEESEHEAD19 campaign. This study finds that LE and water vapor variance is largest at the large-eddy scale in PBL and at the mesoscale. In contrast, vertical velocity variance is primarily present in turbulent and large-eddy scales in PBL. This study confirms the significant role of the large-eddy scale in PBL in contributing to the majority of the vertical moisture transport from the surface to the PBL top. These findings provide better insight into the factors influencing LE at different scales.

1. Introduction

Water vapor and latent heat flux (LE) in the planetary boundary layer (PBL) play critical roles in atmospheric dynamics, the hydrological cycle, radiation balance, and conversion of latent heat (Garratt, 1994; Hu et al., 2023;

Investigation: Guo Lin, Zhien Wang, Yufei Chu, Ming Xue, Kang Yang

Methodology: Guo Lin, Zhien Wang, Yufei Chu, Sreenath Paleri, Ankur R. Desai

Project Administration: Zhien Wang, Conrad L. Ziegler, Xiao-Ming Hu, Ming Xue, Ankur R. Desai

Resources: Zhien Wang, Ankur R. Desai

Supervision: Zhien Wang

Validation: Guo Lin, Yufei Chu

Visualization: Guo Lin

Writing – original draft: Guo Lin

Writing – review & editing: Zhien Wang, Yufei Chu, Conrad L. Ziegler, Xiao-Ming Hu, Ming Xue, Bart Geerts, Sreenath Paleri, Ankur R. Desai, Kang Yang, Min Deng, Jonathan DeGraw

Kiemle et al., 2007; Linné et al., 2006; Pielke et al., 2003; Stevens & Bony, 2013; Stull, 2015). Relevant processes include surface evapotranspiration, transport and diffusion through the PBL, and cloud formation and dissipation (Betts, 1982; LeMone et al., 2019). The PBL, where the mixing process by turbulent eddies at different scales plays a critical role, transports water vapor from the surface to the free atmosphere. LE in the PBL originates from the surface via evapotranspiration, modulated by the entrainment of air in the free troposphere, and PBL circulation and evolution (Linné et al., 2006). However, the land surface heterogeneity across multiple properties drives spatial variability of the vertical transport at various scales in a nonlinear fashion (Avissar & Schmidt, 1998; Platis et al., 2017; Raupach & Finnigan, 1995). Depending on the relative magnitude of the surface and entrainment fluxes, the idealized water vapor flux profile within the well-mixed convective boundary layer (CBL) either decreases or increases with height, in a linear fashion (Stull, 1988). Bange et al. (2002), investigated heat fluxes using airborne flux measurements in the CBL, finding linear profiles of sensible heat flux but not LE. Water vapor and LE measurements are crucial to understanding water vapor transport and its variability in PBL. Although the importance of water vapor is well recognized, its spatial and temporal variability is still poorly characterized by observations, making model validation difficult (Bou-Zeid et al., 2020; Butterworth et al., 2021; Eder et al., 2015; Linné et al., 2006; Mauder et al., 2020; Metzger et al., 2021; Wolf et al., 2017). Accurate accounting of land-atmosphere interactions is critical for improving the performance of numerical weather and climate prediction models (Pielke et al., 1997).

Water vapor variability on scales has a significant impact on cloud and precipitation development, but it has not yet been fully understood and characterized comparable to the finest resolutions of climate and weather models due to the atmospheric responses from energy balance on land surface heterogeneity (Fischer et al., 2013; Sherwood et al., 2010; H. Wang et al., 2010). The land surface is usually heterogeneous over a wide range of spatial scales due to variability in (among other parameters) vegetation, terrain, soil texture and wetness, cloud cover, and urban areas (Desai et al., 2005; Desai, Paleri, et al., 2022; Mahrt, 2000). However, measurements at a single location, such as eddy correlation flux towers, are often used to represent the properties of a larger region. Individual point sensors may not be representative in complex terrain or in varied vegetation (Bou-Zeid et al., 2020; Butterworth et al., 2021; Mauder et al., 2020).

While most horizontal humidity transport occurs through advection on large scales and is well resolved in atmospheric models, vertical transport is dominated by turbulence on sub-grid scales and must be parameterized (Kiemle et al., 2007). The vertical transport of water vapor generated by surface forcings from the heterogeneous land surface at multiple scales leads to the scale-dependent atmospheric variability (Avissar & Schmidt, 1998). Water vapor transport is a complex natural multiscale process that requires scale-based parameterizations because it is hard to resolve all the relevant spatial information directly in numerical simulations or through observations (Pressel et al., 2014). The lack of understanding of the small-scale dynamics of water vapor throughout the PBL leads to strong limitations in predicting localized phenomena in weather models (Couvreur et al., 2005; Hill et al., 2008, 2011; Steinfeld et al., 2007). As such, the multiscale nature of water vapor has continued to defy a generalized approach or theory for “characterizing” its impact on the PBL (Mahrt, 2000). Heat and moisture exchange measurements between the land surface and the atmosphere are critical to understanding the causes of variability in the PBL.

The eddy covariance (EC) technique is widely used to estimate the energy exchange between the surface and the atmosphere at a single location: water vapor fluxes are estimated from the covariance of the water vapor and vertical velocity fluctuations (Aubinet et al., 2012). The water vapor flux ($\text{g kg}^{-1} \text{ m s}^{-1}$) is the covariance of w (m s^{-1}) and r_v (g kg^{-1}). This flux translates into the LE (W m^{-2}) by multiplying the air density and the latent heat of water vaporization. The LE is a valuable tool for monitoring changes in local sources and sinks of water vapor subjected to local influences at a fixed station over an extended period. The EC technique suffers from certain limitations in covering the full spectrum of the atmospheric transport (Finnigan et al., 2003; Mauder et al., 2007). The assumption of stationary and horizontal homogeneity to calculate turbulent fluxes in the EC technique can complicate sampling flux contribution from the low frequencies. A sufficiently long averaging interval is required to minimize the spectral loss in the low-frequency part. Non-local mesoscale eddies might either be geographically fixed to a surface heterogeneity or slowly moving in weak wind conditions (Mahrt, 1998). Traditional EC calculation approaches are usually inadequate for capturing mesoscale features associated with the surface heterogeneity (Butterworth et al., 2021; Charuchittipan et al., 2014; Foken et al., 2011; Gao et al., 2016).

The mesoscale forcing is not adequately resolved by traditional EC measurement due to short averaging times, surface heterogeneity, PBL circulation, and lack of closure in the energy budget (Butterworth et al., 2021; Charuchittipan et al., 2014; Foken et al., 2011; Mahrt, 2010; Mauder et al., 2006; X.-M. Sun et al., 2006). Hence

the expected value from a single-tower measurement tends to systematically underestimate the surface heat flux. Compared to shortcomings in conventional EC measurements, large eddy simulation (LES) studies can advance the understanding of scale-dependent physical processes in fluxes that EC tower measurements cannot resolve. Margairaz et al. (2020) investigated organized PBL circulations over the heterogeneous surface over a broad range of atmospheric stability conditions in LES. Couvreux et al. (2005) used airborne measurements and LES to investigate r_v variability in the PBL at the large-eddy scale and sub-mesoscale (a few kilometers) in the CBL. The vertical transport associated with the large eddy to mesoscale circulations could be missed by single tower-based measurements, and it can be overestimated if the tower happens to be located near mesoscale boundaries (Charuchittipan et al., 2014; Helbig et al., 2021; Mahrt, 2010).

Airborne measurements offer the advantage of sampling spatial variability compared to ground-based in situ tower measurements (Desjardins et al., 1995). Aircraft can cover mesoscale eddies during one flight, making it favorable for investigating atmospheric mesoscale motions, while ground-based towers passively detect eddies with scales calculated by the mean wind (Mauder et al., 2007). The ground-based towers usually need 30-min flux-averaging periods to capture low-frequency contributions to the fluxes (Aubinet et al., 2012; Charuchittipan et al., 2014; X.-M. Sun et al., 2006). Spatial sampling coverage from micro- γ scale (<20 m) to meso- β scale (up to 200 km) can be provided by high-frequency instruments aboard an aircraft flying in the surface layer (the scale classification is based on Orlanski (1975), Mauder et al. (2007), and Paleri et al. (2022)). Recent projects with airborne flux measurements include the Boreal Ecosystem-Atmosphere Study (BOREAS, Sellers et al., 1995), the Northern Hemisphere Climate Processes Land-Surface Experiment (NOPEX, Halldin et al., 1999), the Lindenberg Inhomogeneous Terrain—Fluxes between Atmosphere and Surface: a Long-term Study (LITFASS-98, Beyrich et al., 2002) and LITFASS-2003 (Beyrich & Mengelkamp, 2006), MAtter fluxes in Grasslands of Inner Mongolia as influenced by stocking rate (MAGIM, Butterbach-Bahl et al., 2011), and ScaleX (Wolf et al., 2017).

The airborne estimation of LE is based on the combination of water vapor with vertical velocity measurements using the EC technique (Linné et al., 2006) and wavelet technique (Mauder et al., 2007; Metzger et al., 2013; Paleri et al., 2022). The EC technique has its limitations and can only be applied to stationary data. Therefore, quality control and assessment are necessary to validate the theoretical assumptions. For example, a stationarity test should be performed on the EC technique for the calculated LE from the airborne measurements (Foken et al., 2004; Y. Sun et al., 2023). However, the wavelet technique can be used to analyze nonstationary data with contributions from different frequencies, especially airborne measurements that span non-homogenous regions (Desjardins et al., 1995; Mauder et al., 2007; Paleri et al., 2022; Torrence & Compo, 1998). Mauder et al. (2007) found that the differences in LE estimations between the EC and wavelet techniques are less than 2%. Differences between aircraft and tower-based estimates of water vapor fluxes are often much larger (Desjardins et al., 1997). Aircraft can serve as extended observation platforms for the scaling up from local (tower-based) to regional estimates of surface-atmosphere energy exchange (Butterworth et al., 2021; Metzger et al., 2021). Although airborne measurements have limitations in sampling duration, frequency, and distance due to operational considerations and high costs (Desjardins et al., 1997; Mauder et al., 2007), the wavelet-based analysis of airborne turbulence data is particularly suited to characterize the water vapor and LE variability in a targeted field experiment.

The present study characterizes the scale-dependence of LE, vertical velocity variance (σ_w^2), and water vapor variance ($\sigma_{H_2O}^2$) at the 100 m above ground level (AGL) flight level in the Chequamegon Heterogeneous Ecosystem Energy-Balance Study Enabled by a High-Density Extensive Array of Detectors 2019 (CHEESEHEAD19) field campaign (Butterworth et al., 2021). The objective is to investigate the spatial-dominant scale of LE, σ_w^2 , and $\sigma_{H_2O}^2$ in the lower PBL and how σ_w^2 and $\sigma_{H_2O}^2$ impact LE variability on diurnal to seasonal scales. Our study examines three hypotheses involving scaled-dependent LE as measured within the PBL during the daytime, based on the literature discussed above:

- *Hypothesis 1:* The spectral characteristics of σ_w^2 and $\sigma_{H_2O}^2$ are different.
- *Hypothesis 2:* σ_w^2 generated by the surface is concentrated across scales less than the PBL height, which is normally below 2 km.
- *Hypothesis 3:* The scale-dependent $\sigma_{H_2O}^2$ includes the contributions of the entrainment of dry air from the free troposphere, and PBL circulation and evolution, which are in large-eddy scale in PBL and even mesoscale.

Ultimately, by contrasting the contributing spatial scales of the LE, σ_w^2 , and $\sigma_{H_2O}^2$, this study leads to a more accurate quantitative assessment of spatially localized contributions from all the relevant transport scales. Section 2 introduces the CHEESEHEAD19 field campaign and reviews the data collection methods, data sets,

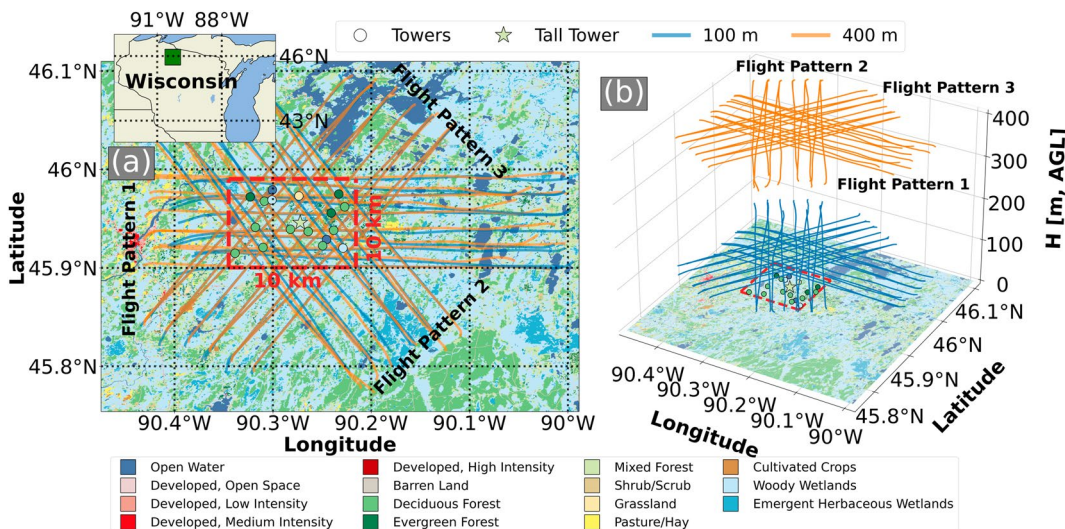


Figure 1. (a) Location of the CHEESEHEAD19 domain (blue square) in Wisconsin (insert map) and colored land classification map from the National Land Cover Database 2019 of the area around the CHEESEHEAD19 domain with three distinct University of Wyoming King Air (UWKA) flight patterns (FPs) at 100 m (blue lines) and 400 m (orange lines); (b) 3D map showing the three UWKA FPs at 100 m (blue lines) and 400 m (orange lines). The red dashed square represents the study domain of flux towers, and the dots and a star indicate the flux tower locations colored by their land cover types.

and instruments. The temporal and spatial variability of LE and how σ_w^2 and σ_{H2O}^2 impact are detailed in Section 3, while discussion and conclusions are presented in Section 4.

2. Data and Methodology

2.1. Experimental Procedure

The CHEESEHEAD19 was an intensive field campaign supported by the National Science Foundation in the Chequamegon-Nicolet National Forest of Wisconsin from June to October 2019 (Butterworth et al., 2021). The experiment intensively sampled land–surface properties and the PBL responses to surface properties across a heterogeneous mid-latitude forested landscape. The land cover within the CHEESEHEAD19 domain is dominated by conifers, deciduous forest, mixed forest, wetlands, and open water, according to the National Land Cover Database (NLCD) 2019 land cover (Figure 1, Dewitz & U.S. Geological Survey, 2021). The canopy heights range from 0 to 35 m, leading to a horizontally heterogeneous surface. This forest, with diverse surface properties varying at multiple scales, was selected to address a crucial gap in our current understanding of surface atmospheric exchanges over a heterogeneous flat land surface (Bou-Zeid et al., 2020).

The CHEESEHEAD field campaign deployed a suite of observing platforms over a core $10 \times 10 \text{ km}^2$ domain (the red dashed domain in Figure 1a) and a $30 \times 30 \text{ km}$ extended domain for airborne measurements. The study domain was partly chosen due to the history of atmospheric science research in the region (Davis et al., 2003; Desai, Murphy, et al., 2022). The EC tower network consisted of 17 flux towers from the National Center for Atmospheric Research (NCAR)—Integrated Surface Flux Station (ISFS) network (colored circles in Figure 1), two additional contributed towers in grassland and a lake, and the Department of Energy Ameriflux regional tall tower (US Pfa/WLEF; the star in Figure 1) (Desai, 2023). A majority of the ISFS sites had flux instruments mounted at 33 m AGL for forests while instruments for wetland, grass, and lake sites were mounted between 1 and 3 m AGL to maintain consistent sampling within homogenous flux footprints (Oncley, 2021). The US Pfa tower has sampled greenhouse gas profiles, meteorological data, and EC flux measurements (energy, carbon, momentum) at 30, 122, and 396 m AGL since 1995 (Berger et al., 2001; Davis et al., 2003). The fluxes were simultaneously measured at 17 points with tower-based systems and short periods with airborne measurements during Intensive Observation Periods (IOPs) (referred to as IOPs henceforth). Thus, the temporal and spatial characteristics of ground-based and airborne measurements complemented each other to evaluate land-atmosphere interactions in PBL at the site and regional scales (Butterworth et al., 2021; Hu et al., 2021; Paleri et al., 2022).

Table 1

Intensive Observation Periods (IOPs), Dates (The M Represents Morning and A Represents Afternoon), RF Numbers and Times, Sunrise and Sunset Times, Flight Patterns, Flight-Level Winds, and Net Radiation of All IOPs

IOP (#)	Date	Flight (#)	Time period (Mor, UTC)	Time period (Aft, UTC)	Sunrise (UTC)	Sunset (UTC)	Fight pattern	Wspd (m s ⁻¹)	Wdir (°)	Rnet (W m ⁻²)
IOP 01	9 July M	RF 01	1413–1616		1121		FP1	6.4	278	495
	9 July A	RF 02		1919–2119		2646	FP1	4.6	271	540
	11 July M	RF 03	1429–1635		1122		FP1	2.9	102	658
	11 July A	RF 04		1922–2127		2644	FP1	6.0	319	633
	12 July M	RF 05	1358–1606		1123		FP1	6.0	318	539
	12 July A	RF 06		1841–2045		2644	FP1	6.2	347	528
	13 July M	RF 07	1428–1631		1124		FP2	5.1	44	626
	13 July A	RF 08		1917–2115		2643	FP3	3.7	71	648
IOP 02	20 August M	RF 09	1358–1611		1206		FP2	6.2	262	164
	20 August A	RF 10		1931–2150		2556	FP2	3.0	150	502
	21 August M	RF 11	1415–1635		1207		FP3	4.7	40	524
	21 August A	RF 12		1918–2137		2555	FP3	6.0	49	479
	22 August M	RF 13	1417–1639		1208		FP3	2.6	134	320
	22 August A	RF 14		1921–2146		2553	FP3	4.4	116	274
	23 August M	RF 15	1414–1637		1209		FP1	3.4	159	509
	23 August A	RF 16		1925–2145		2551	FP1	4.3	184	536
IOP 03	24 September M	RF 17	1359–1635		1247		FP2	6.4	260	356
	24 September A	RF 18		1919–2139		2452	FP2	6.9	280	244
	25 September M	RF 19	1448–1708		1248		FP3	7.6	8	433
	25 September A	RF 20		1936–2152		2450	FP3	9.2	343	159
	26 September M	RF 21	1413–1634		1250		FP2	4.4	278	359
	26 September A	RF 22		1852–2114		2448	FP2	7.2	338	314
	28 September M	RF 23	1444–1705		1252		FP1	3.2	104	464
	28 September A	RF 24		1915–2134		2444	FP1	4.0	107	349

2.2. Airborne Observations

The airborne observations aimed to examine PBL responding to spatial heterogeneous land cover. The University of Wyoming King Air (UWKA) aircraft was equipped with a suite of atmospheric measurement probes, including wind, temperature, and humidity measurements up to 25 Hz to estimate turbulent fluxes (French et al., 2021). The UWKA used a high-precision geo-positioning system (Trimble/Applanix, model POS AV410) and gust probe to obtain 3D position and 3D velocity information, including horizontal wind speed (*Wspd*), horizontal wind direction (*Wdir*), and *w* used in this study (Haimov & Rodi, 2013). The r_v was measured by a LI-COR LI-7000 CO₂/H₂O analyzer. The sampling frequency of *w* and r_v was 25 Hz, and the aircraft flew at a true air speed of ~90 m s⁻¹. Net radiation (*Rnet*) data were also collected to provide information on theoretical maximum latent plus sensible heat fluxes. The UWKA also sampled 2D vertical profiles of water vapor, aerosols, and temperature below the flight level using a nadir-pointing Compact Raman Lidar (CRL, Lin et al., 2019, 2023; Liu et al., 2014; Z. Wang, 2020; Wu et al., 2016) and aerosols with the zenith-pointing Wyoming Cloud Lidar (Lin et al., 2021; Z. Wang et al., 2009) at 400 m height. Three IOPs with the UWKA were conducted during the experiment in each month from July to September (details in Table 1). The flight consisted of two 3-hr flights for each research flight (RF in Table 1), one in the morning (14:00–17:00 UTC; odd numbers in RF, using M as morning) and another in the afternoon (19:00–22:00 UTC; even numbers in RF, using A as afternoon). The flight times relative to sunrise and sunset differ in RFs and months (Table 1). Three flight patterns (FPs) were conducted in IOPs (oriented W–E for FP1; NW–SE for FP2, SW–NE for FP3 in Figure 1 and Table 1) based on a flux heterogeneity optimization approach (Metzger et al., 2021).

During the UWKA RFs, the aircraft flew a ~30 km leg at 400 m AGL (orange flight tracks in Figure 1) to sample the temperature, aerosols, and moisture profiles of the PBL with the CRL. The UWKA then flew a ~30 km leg back at 100 m AGL (blue flight tracks in Figure 1) to measure turbulent fluxes at flight level. The 400 and 100 m flights were repeated 10 times in every RF. The 100 m altitude was the lowest altitude deemed safe to fly within the surface layer as the canopy height extended to 35 m. The choice of FP was based on the prevailing wind direction: the one closest perpendicular to the prevailing wind was chosen (Metzger et al., 2021). The flight legs extended an average of 10 km beyond the core domain to maximize data coverage under different wind conditions and the number of independent atmospheric eddies observed by the aircraft EC measurements. The 30 km flight legs captured enough eddies and mesoscale variation to properly compute eddy correlation statistics for fluxes using the wavelet decomposition method (Mauder et al., 2007; Paleri et al., 2022). Although the CHEESEHEAD19 data set provided good spatial coverage but with limited temporal coverage (72 flight hours in 12 days, all with fair-weather conditions), it remains one of the largest airborne flux measurement data sets collected to date.

2.3. Wavelet Flux Analysis and Equations

2.3.1. Wavelet Scalogram and Variance

A wavelet transform can be used to evaluate the scale-depended contribution of atmospheric fluxes from aircraft measurements (Attie & Durand, 2003; Mauder et al., 2007; Paleri et al., 2022; Strunin & Hiyama, 2005; Vadrevu & Choi, 2011). The wavelet functions and analysis methods were developed for time-frequency analysis revealing localized information (Farge, 1992; Thomas & Foken, 2004). The wavelet analysis is a powerful mathematical tool that, based on the ergodic hypothesis, does not require data to be stationary at many different frequencies (Mauder et al., 2007; Strunin & Hiyama, 2005; Torrence & Compo, 1998), unlike other conventional methods such as a Fourier transform (Foken & Wichura, 1996). In this regard, the wavelet analysis is particularly suitable for aircraft data measured above heterogeneous terrain to calculate atmospheric fluxes on different scales during the CHEESEHEAD19 field campaign.

The existing wavelet methodology is expanded to facilitate space-scale analysis of the UWKA in-situ data from Torrence and Compo (1998) and Mauder et al. (2007). The Morlet wavelet, $\Psi(n) = \pi^{-\frac{1}{4}} e^{i\omega_0 n} e^{-\frac{n^2}{2}}$, has been selected as the mother wavelet in the field of atmospheric turbulent studies, due to its good localization in space and frequency domains (e.g., Mauder et al., 2007; Paleri et al., 2022; Torrence & Compo, 1998). The Morlet wavelet is defined via a non-dimensional space parameter n in a discrete sequence $x(n)$ with N data points, where ω_0 is the nondimensional frequency with the value of 6 to satisfy the admissibility condition from Farge (1992) and Torrence and Compo (1998). The wavelet coefficients that used the mother wavelet take the form:

$$W_x(a, b) = \sum_{n=0}^N x(n) \Psi_{p,a,b}^*(n) \quad (1)$$

where a is the scale or dilatation parameter, b is the space or translation parameter, and $\Psi_{p,a,b}^*$ is the complex conjugate of the mother wavelet given by:

$$\Psi_{p,a,b} = \frac{1}{a^p} \Psi\left(\frac{n-b}{a}\right) \quad (2)$$

The normalization factor $p = 1/2$ is used in this study. Application of the Morlet wavelet function used in the wavelet transform produces a complex number as its output. By squaring the transformed wavelet coefficients, the wavelet scalogram is obtained as $|W_x(a_j, b_j)|^2$ (Torrence & Compo, 1998). The scale parameter, a , relates to n in distance/time along the flight track while the space parameter, b , relates j in scale. The scales can be defined in terms of power:

$$a_j = a_0 2^{j\delta j}, j = 0, 1, \dots, J \quad (3)$$

$$J = \delta j^{-1} \log_2\left(\frac{N\delta t}{a_0}\right) \quad (4)$$

where a_0 is the smallest resolvable scale; δj is a nondimensional factor with a value of 0.04 that determines the spacing between discrete scales of the wavelet transform; and J is the largest scale. The time interval $\delta t = 0.04$ s

for the 25 Hz flight-level data, while $a_0 = 2\delta t$ is the Nyquist frequency in scale. (Torrence & Compo, 1998). The variance takes form (Hudgins, 1992):

$$\sigma_x^2 = \frac{\delta j \delta t}{C_\delta} \frac{1}{N} \sum_{j=1}^{j_2} \sum_{n=n_1}^{n_2} \frac{|W_x(a_j, b_n)|^2}{a_j} \quad (5)$$

where

$$0 \leq n_1 \leq n_2 \leq N - 1$$

$$0 \leq j_1 \leq j_2 \leq J$$

The factor C_δ is the reconstruction factor with a value of 0.776 for the Morlet wavelet (Torrence & Compo, 1998). If $n_1 = 0$, $n_2 = N - 1$, $j_1 = 0$, and $j_2 = J$, the σ_x^2 represents the variance of the flight-level data that is calculated as the sum over all scales because the wavelet spectrum of flight-level data is analogous to a Fourier spectrum. This study also uses the normalized scaled dependent variance to investigate the scale contribution and ignorant magnitude variations among flight legs.

$$\hat{\sigma}_x^2 = \frac{\frac{\delta j \delta t}{C_\delta} \frac{1}{N} \sum_{j=1}^{j_2} \sum_{n=0}^{N-1} \frac{|W_x(a_j, b_n)|^2}{a_j}}{\frac{\delta j \delta t}{C_\delta} \frac{1}{N} \sum_{j=0}^J \sum_{n=0}^{N-1} \frac{|W_x(a_j, b_n)|^2}{a_j}} = \frac{\sum_{j=1}^{j_2} \sum_{n=0}^{N-1} \frac{|W_x(a_j, b_n)|^2}{a_j}}{\sum_{j=0}^J \sum_{n=0}^{N-1} \frac{|W_x(a_j, b_n)|^2}{a_j}} \quad (6)$$

The cumulated value of normalized scaled variance equals 1.

2.3.2. Wavelet Cross-Scalogram and Covariance

The wavelet cross-scalogram is similar to the scalogram and is defined as $W_x(a, b) W_y^*(a, b)$. The complex conjugate $W_y^*(a, b)$ is the wavelet transform of another variable. Similarly, the covariance of two variables can be calculated via the expression:

$$\text{cov}_{xy} = \frac{\delta j \delta t}{C_\delta} \frac{1}{N} \sum_{j=j_1}^{j_2} \sum_{n=n_1}^{n_2} \frac{W_x(a_j, b_n) W_y^*(a_j, b_n)}{a_j} \quad (7)$$

The covariance is the real part of the scalogram, which is often used in meteorology to study spectral contributions to turbulent fluxes (Stull, 1988). For example, the water vapor flux ($\text{g kg}^{-1} \text{ m s}^{-1}$) is the covariance of x and y as x equals w (m s^{-1}) and y equals r_v (g kg^{-1}). This present study translates the water vapor flux into the LE (W m^{-2}) by multiplying the air density and the latent heat of water vaporization. Similarly, the normalized covariance of two variables is defined by an expression of the form:

$$\hat{\text{cov}}_{xy} = \frac{\sum_{j=j_1}^{j_2} \sum_{n=0}^{N-1} \frac{W_x(a_j, b_n) W_y^*(a_j, b_n)}{a_j}}{\sum_{j=0}^J \sum_{n=0}^{N-1} \frac{W_x(a_j, b_n) W_y^*(a_j, b_n)}{a_j}} \quad (8)$$

To see the scale-resolved σ_x^2 and σ_y^2 contributing to the scale-resolved covariance, the scale-resolved covariance between x' and y' is calculated by the variance decomposition equation:

$$\text{cov}_{(x,y)}(j) = k \times \sqrt[2]{\sigma_x^2(j)} \times \sqrt[2]{\sigma_y^2(j)} \quad (9)$$

where k is the normalized parameter to adjust the $\text{cov}_{(x,y)}$ with the same maximum value to scale-dependent covariance distribution on the scale calculated by Equation 9. Note that the quantity $\text{cov}_{(x,y)}$ is non-negative, but cov_{xy} from Equation 7 is calculated by the real part of $W_w(a_j, b_n) W_{H2O}^*(a_j, b_n)$, which could have negative values on scales.

The wavelet spectrum and co-spectrum depend on the scale-dependent bin size, but variance (Equation 5) and covariance (Equation 7) are independent of bin size, since they are normalized by bin size. Mauder et al. (2007) show examples of covariance calculated by the wavelet technique from airborne in situ measurements and scale-resolved distributions in their Figure 4. In this study, the wavelet technique is used to calculate and evaluate the 100 m flight-level scale-resolved distribution and temporal variation of LE, σ_w^2 , and σ_{H2O}^2 for all flight legs

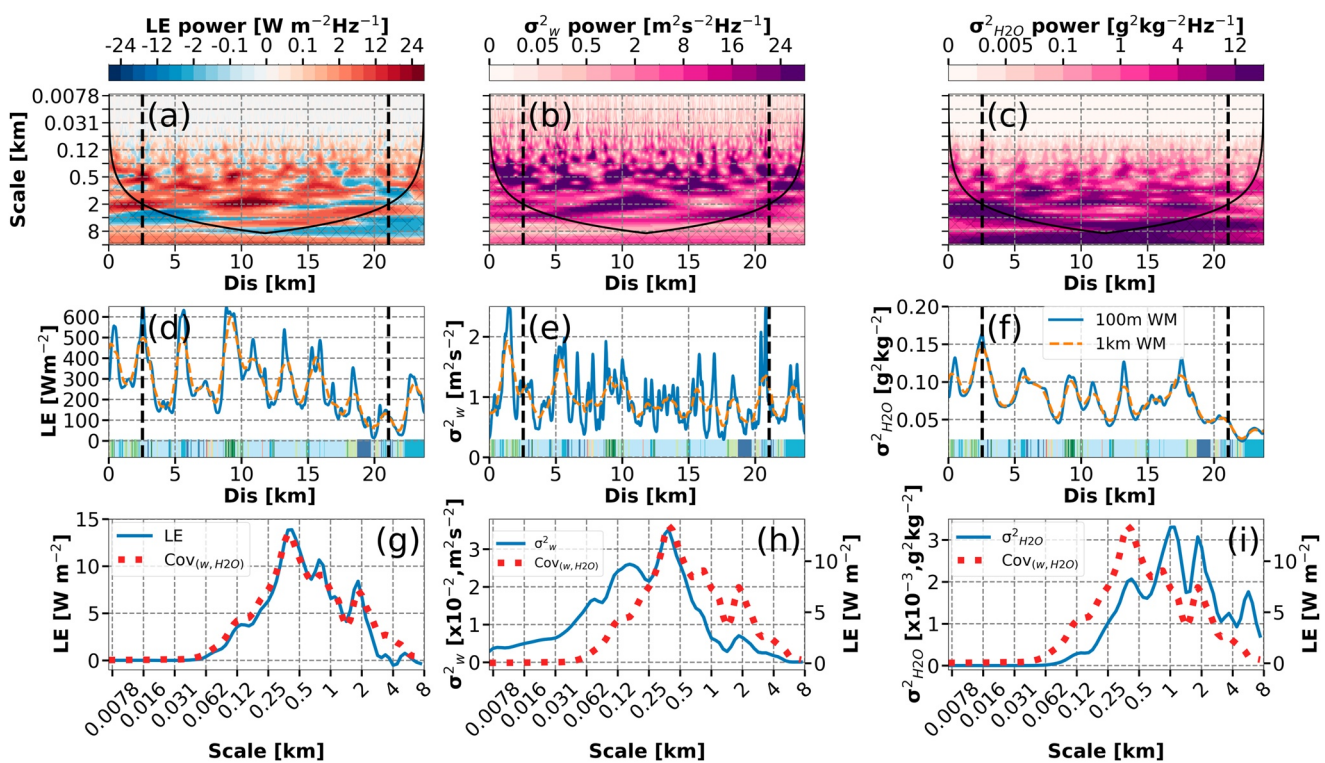


Figure 2. A sample wavelet cross-scalogram between w and r_v in the result of (a) LE power; the wavelet scalogram of (b) σ_w^2 power and (c) σ_{H2O}^2 power illustrating the scale-resolved spatial contributions along RF02 flight leg 2 at 100 m above ground level. The (d) scale-integrated LE, (e) σ_w^2 , and (f) σ_{H2O}^2 along the flight tracks are calculated by integrating scalogram in spatial scales along the y-axis of panels (a–c), respectively. The spatial LE, σ_w^2 , and σ_{H2O}^2 are smoothed by 28-point average windows (100 m; blue lines), and 278-point averaged windows (1 km; orange lines) in panels (d–f). The (g) scale-dependent LE, (h) σ_w^2 , and (i) σ_{H2O}^2 are averaged over the flight leg between $2.5 < x < 21$ km (within two vertical black lines shown in panels (a–f)). The $\text{cov}_{(w, H2O)}$ is calculated by the variance of r_v and the variance of w by Equation 9. Hashed portions in panels (a–c) below the black line represent the cone of influence (COI) of edge effects. The vertical black lines represent the threshold of 2 km influenced by COI for the chosen flight segment to calculate scale-dependent LE, σ_w^2 , and σ_{H2O}^2 . The colored land classification map along the flight track is shown at the bottom of panel (d–f).

from the July, August, and September IOPs (Table 1). The normalized scale-resolved LE, σ_w^2 , and σ_{H2O}^2 calculated by Equations 6 and 8 are used to analyze the relative scale-dependent contribution from σ_w^2 and σ_{H2O}^2 to LE regardless of their values. The spatial scale is transformed by multiplying the time scale (j) by the mean ground speed ($\sim 90 \text{ m s}^{-1}$) of each flight leg for 25 Hz flight-level data.

2.3.3. Example of Wavelet Variance and Covariance

The wavelet method permits to allocate the information about flux contributions from the entire flight track to a specific subsegment of that track. We apply wavelet calculation to the same flight track of Figure 3 in Paleri et al. (2022) for comparison and to ensure consistent calculation (Figure 2). The wavelet technique is applied to calculate the wavelet power co-spectrum of LE (LE_{WT}), and the wavelet power spectra of w and r_v (Figures 2a–2c). We also calculated LE using Equation 7, and $\sigma_w^2 (\text{m}^2 \text{s}^{-2})$ and $\sigma_{H2O}^2 (\text{g}^2 \text{kg}^{-2})$ using Equation 5 with 100 m flight-level data for spatial and scale analysis (Figures 2d–2i). The hashed areas shown in Figures 2a–2c are the cone of influence (COI) where edge effects due to discontinuities at the endpoints become important. Since the wavelet decomposition deals with finite-length flight leg, errors will occur at the beginning and end of the wavelet power spectrum (Torrence & Compo, 1998).

Spatial variations of LE, σ_w^2 , and σ_{H2O}^2 were calculated by normalizing power spectra and the co-spectrum with scale-dependent bin size and integrating the scale up to 8 km along the flight-track segment (Figures 2d–2f) since the integrated processes covering the full-range scale may introduce uncertainties by the COI. The 1 km window-averaged LE varies from 60 to 600 W m^{-2} in a 28 km flight track. The land classification is mapped out at the bottom of Figures 2d–2f. The spatial LE is related to surface heterogeneity, with the lowest LE occurring at 18 km over water along the flight track. The maximum 600 W m^{-2} latent heat flux at 9 km coincides with the cross-scalogram of LE power contribution up to 4 km (Figure 2a). However, the high value of LE does not correlate

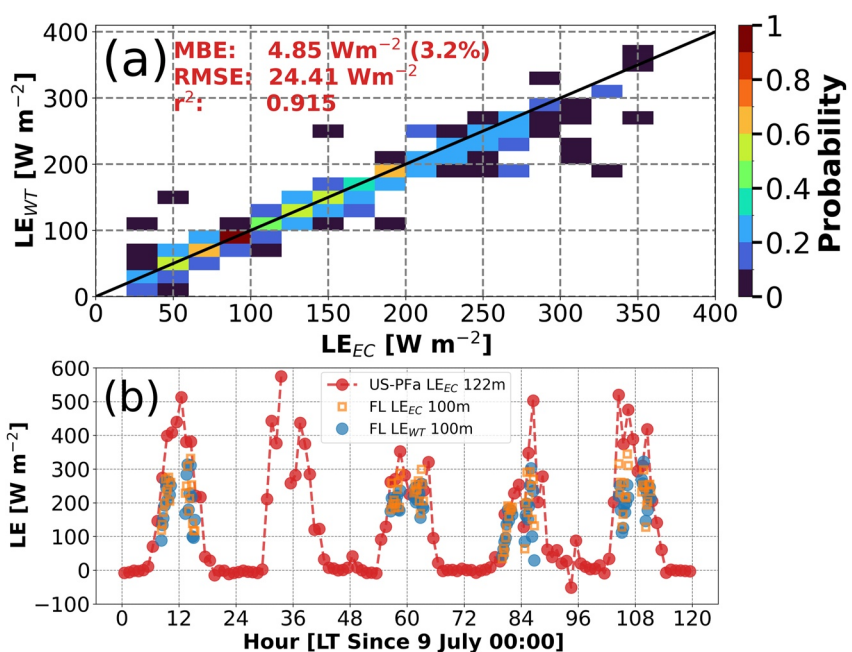


Figure 3. (a) Comparison of airborne flight-level LE_{WT} and LE_{EC} for all 100 m flight legs during all three Intensive Observation Periods (IOPs) (Table 1); (b) comparison of leg-averaged LE_{WT} at 100 m flight level and LE_{EC} at 122 m on the US PFa tall tower for the July IOP. The flight-level LE_{WT} is represented by blue circles and flight-level LE_{EC} is represented by orange squares. The 122-m tall-tower LE_{EC} is calculated by the eddy covariance technique.

to only high σ_w^2 or high $\sigma_{H_2O}^2$, but instead to the covariance of σ_w^2 and $\sigma_{H_2O}^2$. The 600 W m⁻² LE at around 9 km is collocated with 1.3 m² s⁻² σ_w^2 and 0.12 g² kg⁻² $\sigma_{H_2O}^2$. Neither σ_w^2 nor $\sigma_{H_2O}^2$ is the maximum value in the segment.

The spatial variations (Figures 2d–2f) along the flight-track segment cannot resolve the scale contribution of σ_w^2 and $\sigma_{H_2O}^2$ to LE clearly. The leg-averaged scale-resolved LE (Figure 2g) reflects the importance of small-scale contributions with values greater than 2 W m⁻² in scales from 100 m to 3 km with a maximum LE of 14 W m⁻² at ~0.4 km. The scale-resolved σ_w^2 with values greater than 5×10^{-2} m² s⁻² is between 16 m and 1.5 km within PBL turbulence scales (<2 km, Figure 2b). The scale-resolved $\sigma_{H_2O}^2$ is concentrated between 200 m and 8 km with a peak of 3.2×10^{-2} g² kg⁻² at 1 km. The distribution of scale-resolved $\sigma_{H_2O}^2$ between 200 m and 8 km could result from large-eddy circulations in PBL and mesoscale forcings. To see the scale-resolved σ_w^2 and $\sigma_{H_2O}^2$ contributing to the scale-resolved LE, the scale-resolved covariance between w' and r_v' [$\text{cov}_{(w, H_2O)}$] is calculated using Equation 9. Note that both the turbulent and most large-eddy scales fall in the inertial subrange for isotropic turbulence in the surface layer. The LE and $\text{cov}_{(w, H_2O)}$ have almost the same distributions in the turbulent and most large-eddy scales. However, mesoscales up to 8 km fall outside the inertial subrange, resulting in a difference between LE and $\text{cov}_{(w, H_2O)}$. The $\text{cov}_{(w, H_2O)}$ is shown in Figures 2g–2i to compare the different scale-resolved distributions among LE, σ_w^2 , and $\sigma_{H_2O}^2$.

2.3.4. Wavelet and Eddy Covariance LEs Comparison

To examine the accuracy of airborne LE calculated by wavelet technique (LE_{WT}) at 100 m, the flight-leg averaged LEs of 240 flight legs calculated by the wavelet technique are compared with leg-averaged LEs from the traditional EC technique (LE_{EC}; the subscripts EC and WT are only shown when comparing fluxes between EC and wavelet techniques) (Figure 3a). Since the influence of edge effects by COI is generally larger toward the ends of the wavelet cross-scalogram (Figure 2a), a threshold of chosen segment legs is in the scale of COI greater than 2 km to ensure a long-enough flight leg to sample mesoscale eddies and to reduce significant edge effects from discontinuities at the endpoints for wavelet LE calculations (i.e., the flight segment between two vertical black lines in Figure 2a). The traditional leg-averaged LE_{EC} is defined (Stull, 1988):

$$\text{LE}_{\text{EC}} = \overline{w' r_v'} \quad (10)$$

where w' and r_v' are the w perturbation and r_v perturbation from leg-averaged values, respectively. The same flight segment is used for LE calculations with the two techniques. The 2D histogram comparing traditional

leg-averaged LE_{EC} against LE_{WT} for the 240 flight legs, shown in Figure 3a, has a bin size of 20 W m^{-2} from 0 to 400 W m^{-2} . The wavelet LE is slightly smaller than the LE_{EC} with a mean bias error of 4.85 W m^{-2} , $\sim 3.2\%$ of the total mean LE_{EC} , and the root mean square error of 30 W m^{-2} . The correlation coefficient (r^2) is 0.915. The low mean differences and high r^2 indicate reliable leg-averaged LE_{WT} compared to the LE_{EC} .

To further evaluate the airborne LE_{WT} , the flight-level LE_{WT} and LE_{EC} at 100 m and the LE_{EC} of tall-tower US-PFa at 122 m are compared (Figure 3b). The comparison of LE is only in July because the tall towers measured inaccurate negative LE_{EC} at 122 m height during the August IOP, while EC LEs at 30 and 396 m were positive. The LE_{EC} in August and September have been excluded from the quality control process. The airborne LE_{WT} compare reasonably well with the airborne LE_{EC} at 100 m height and the one-hour averaged US PFa LE_{EC} at 122 m height. However, the flight-level LE_{WT} do not match the LE_{EC} at the flight level and US PFa tower height. The difference between airborne wavelet LEs and airborne LE_{EC} may be due to the fact that LE_{WT} only consider the scales from 8 m to 8 km. The US PFa LEs are one-hour averaged LE_{EC} . The one-hour mean EC LEs account for a footprint of 10–23 km, given the $2.9\text{--}6.4 \text{ m s}^{-1}$ averaged wind speeds (Table 1), while the airborne wavelet-calculated LE represents about 23–30 km spatial distance in 5 min. The tower measurements at a fixed point only represent a small area around the flux tower in the footprint flux map (Figure 12 in Butterworth et al. (2021)). The differences between the LEs obtained from the fixed-point tall tower and moving airborne measurements could be their different spatial coverages. LEs measured by aircraft represent contributions from local heterogeneities and mesoscale forcings (scales $>2 \text{ km}$) from the $30 \times 30 \text{ km}^2$ domain as sampled by aircraft measurements. The fixed-point tall tower results represent the smaller area around it and advected from the upper wind, compared to the wider area covered by aircraft measurements (Figure 12 in Butterworth et al., 2021).

3. Results

3.1. Surface Flux Variability Measured by Flux Towers

Seventeen ISFS flux towers provide continuous spatial flux records in the CHEESEHEAD19 domain throughout the campaign from July to September (locations in Figure 1). Surface heterogeneity influences the surface energy balance and resulting atmospheric responses in LE variations. The full-monthly mean (30/31 days averaged value) R_{net} , ground heat flux (G_{sf}), sensible heat fluxes (H), LE are calculated between 13:00 and 00:00 UTC (UTC—5 hours for Central Daylight Time or Local Time) to provide daytime fluxes in July, August, and September, since the latest sunrise and earliest sunset time were 12:52 and 00:44 UTC on 28 September, respectively (all sunrise and sunset time shown in Table 1). The spatial incoming available energy ($R_{net} + G_{sf}$) varied from 425 to 290 W m^{-2} in July, from 350 to 270 W m^{-2} in August, and from 230 to 130 W m^{-2} in September in a $10 \times 10 \text{ km}^2$ domain (Figure 4). The LE varied from 235 to 85 W m^{-2} in July, from 190 to 95 W m^{-2} in August, and from 120 to 20 W m^{-2} in September. These spatial variabilities of fluxes in the $10 \times 10 \text{ km}^2$ domain could come from the heterogeneous forested landscape, the topography of the surface, and atmospheric responses from surface forcing. This deployment strategy reveals the variation in surface and vegetation properties across the CHEESEHEAD19 domain. The tower-monthly mean of incoming available energy and LE decreased from July to September (the last column in Figure 4). The sum of incoming available energy exceeds surface H and LE, which leads to the energy balance closure problem. The extended 3-month duration of the field experiment allows us to sample the seasonal shift in the surface energy budget partitioning as the study domain shifts from a LE-dominated late summer landscape to a greater sensible heat contribution early autumn landscape (Butterworth et al., 2021).

3.2. LE Variability

3.2.1. The Temporal Variability of Leg-Averaged LE

The leg-averaged LEs at the 100 m flight level reveal temporal variabilities. The leg-averaged LE is calculated by both wavelet (blue dots; by Equation 7) and EC (red squares; by Equation 10) techniques for every flight leg on both morning and afternoon RFs (Figure 5). The wavelet LEs are generally in good agreement with EC LEs through time. The RF-average LE ranged from 250 W m^{-2} (12 July M and 22 August A) to 50 W m^{-2} (20 August M and 28 September A) (Figure 5). These spatiotemporal variations reflect different surface types, wind conditions, and net radiation variations with time (Figure 1 and Table 1). The mean values of RF LE indicate a decreasing trend from 210 to 80 W m^{-2} from July to September (Figure 5). In summary, the leg-averaged LE decreased from July to September, but the diurnal and synoptic variations of LEs cannot be ignored.

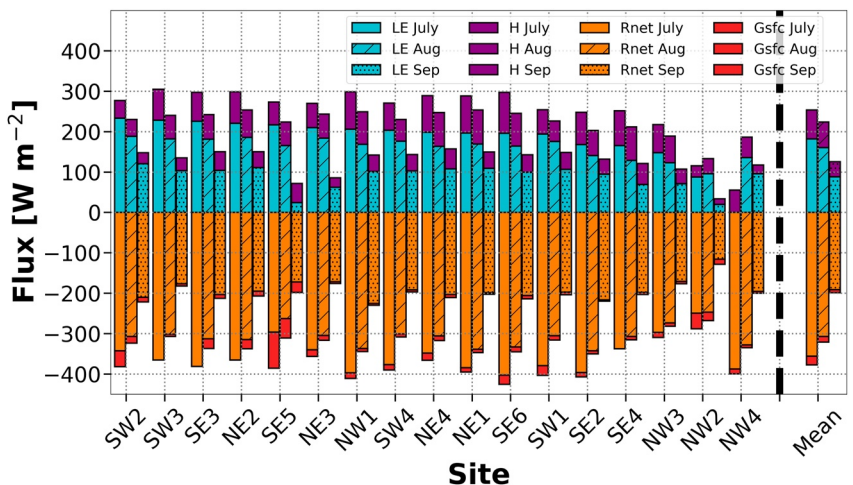


Figure 4. The monthly averaged daytime (13:00–00:00 UTC) LE, H, net radiation (Rnet), and ground heat flux (Gsfc) from the 17 eddy covariance towers and the 17-station mean values in July, August, and September. The sites are ordered with July LEs. Bad data were reported for relative humidity measurements, thus, there was no LE available in July at site NW4.

3.2.2. The Temporal Variability of Scale-Resolved LE

The scale-resolved LE is calculated by Equation 7 for all flight legs to determine the scale contribution to the total LE over time and location. We examine all 12 days (Table 1), 4 from each IOP, each with a morning and an afternoon flight (Figure 6). The morning measurements include the first 10 flight legs, while the afternoon measurements consist of the last 10 flight legs in each day (Figure 6, separated by black dashed lines). The scale-resolved LE is averaged in each flight leg and is mostly between 62 m and 8 km as shown in Figure 6. The scale-resolved LE increases with time (leg number) as the total LE increases in the morning of 09 July, 12 July, 22 August, and 24 September, while it decreases in the afternoon of 09 July, 20 August, 22 August, and 26 September. However, these patterns are inconsistent for all dates, indicating the significant roles of PBL circulation and mesoscale advection in controlling local LEs other than radiation. The daily temporal variation of total LE varies from 50 W m⁻² (28 September) to 270 W m⁻² (12 July). Although the total and scale-resolved LEs indicate strong temporal variation with legs, the primary scale is from 200 m to 4 km.

3.3. The Contributions of w' and r_v' on Scale-Resolved LE

3.3.1. Total LE Dependency

The scale-resolved LEs are composited at various total LEs ranging from 10 to 270 W m⁻² in 20 W m⁻² increments. The scale dependencies of LE, σ_w^2 , and σ_{H2O}^2 from 7.8 m to 8 km are depicted in Figures 7a–7c. The

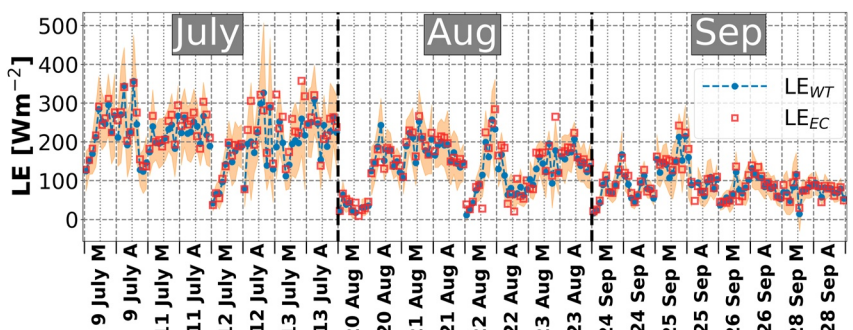


Figure 5. The leg-averaged LE was calculated by wavelet technique (blue dots) with their standard deviation (orange shaded area) and eddy covariance technique (red squares) on legs. The orange-shaded areas represent the standard deviations of the LE_{WT} within the leg indicating spatial variabilities. The fitted line shown as the blue line represents the trend of the leg-averaged LE in RFs from July to September.

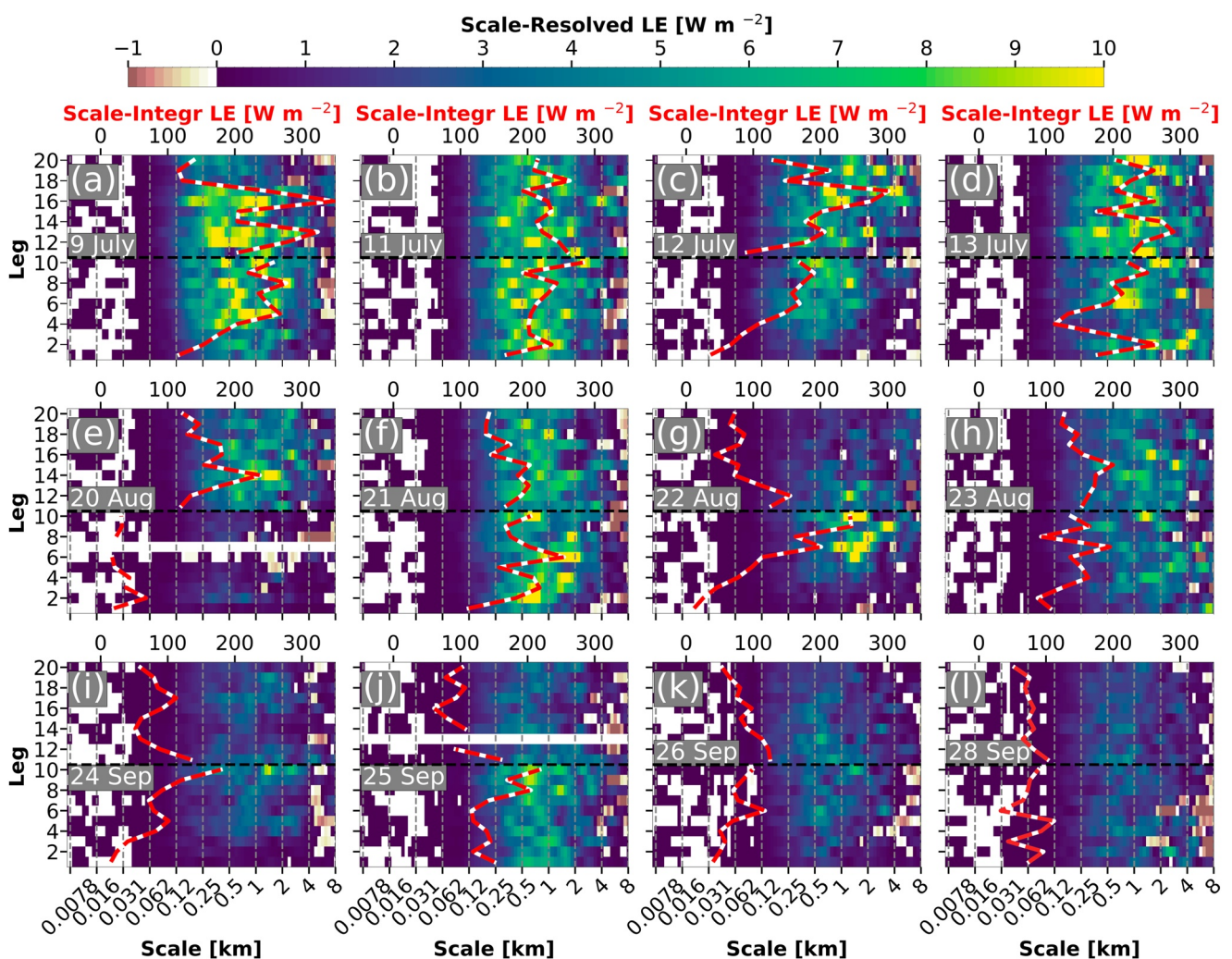


Figure 6. The leg-averaged LE distributions on the scale (x-axis) and leg number (y-axis) for dates of (a) 9, (b) 11, (c) 12, and (d) 13 July; (e) 20, (f) 21, (g) 22, and (h) 23 August; (i) 24; (j) 25; (k) 26, and (l) 28 September. Legs 1–10 are for the morning and Legs 11–20 are for the afternoon. The red-dashed lines represent the total LE (scale on upper x-axis). The flight legs cover distances between 25 and 30 km. The red-dashed lines represent the total LE.

distribution of scale-resolved LEs with values greater than 0.5 W m^{-2} range from 200 m–1.5 km to 100 m–8 km, with the maximum scale-resolved LE increasing from 0.5 to 8 W m^{-2} as the total LE linearly increases from 20 to 260 W m^{-2} (white dashed contours in Figure 7a). Compared to the scale-resolved LE distributions, the scale-resolved σ_w^2 with values greater than $0.25 \times 10^{-2} \text{ m}^2 \text{ s}^{-2}$ is in smaller scale ranges from 50–700 m to 16 m–4 km. The scale-resolved $\sigma_{\text{H}_2\text{O}}^2$ distribution with a value greater than $2 \times 10^{-4} \text{ g}^2 \text{ kg}^{-2}$ mainly focuses from 400 m–8 km to 150 m–8 km in scale as the total LE increases from 20 to 260 W m^{-2} . As the total LE increases, the scale-resolved LE, σ_w^2 , and $\sigma_{\text{H}_2\text{O}}^2$ distributions extend to broader ranges. For LE increases between 20 and 100 W m^{-2} , the total σ_w^2 (red dashed line in Figure 7b) quadruples (from 0.24 to $1.04 \text{ m}^2 \text{ s}^{-2}$), while the total $\sigma_{\text{H}_2\text{O}}^2$ (red dashed line in Figure 7c) remains steady (around $0.02 \text{ g}^2 \text{ kg}^{-2}$). The total σ_w^2 is nearly constant between 0.8 and $1.00 \text{ m}^2 \text{ s}^{-2}$ as the total LE increases from 100 to 260 W m^{-2} . However, the total $\sigma_{\text{H}_2\text{O}}^2$ linearly increases from 0.018 to $0.048 \text{ g}^2 \text{ kg}^{-2}$ from 100 to 220 W m^{-2} . The characteristics of σ_w^2 and $\sigma_{\text{H}_2\text{O}}^2$ variations show the dominance of σ_w^2 for low LE periods and the dominance of $\sigma_{\text{H}_2\text{O}}^2$ for high LE periods.

It is difficult to investigate the relative scale contributions of σ_w^2 and $\sigma_{\text{H}_2\text{O}}^2$ to LE due to their value and scale-range variations as the total LE increases in Figures 7a–7c. To address this issue, the scale-resolved LE, σ_w^2 , and $\sigma_{\text{H}_2\text{O}}^2$ are normalized based on Equations 6 and 8. The 50% value in the cumulative normalized scale-resolved LE, σ_w^2 , and $\sigma_{\text{H}_2\text{O}}^2$ are marked as blue dashed lines (Figures 7d–7f). The distribution of normalized scale-resolved LE with values greater than 2% shifts from 120 m–1.5 km to 250 m–2.2 km as the total LE increases from 20 to

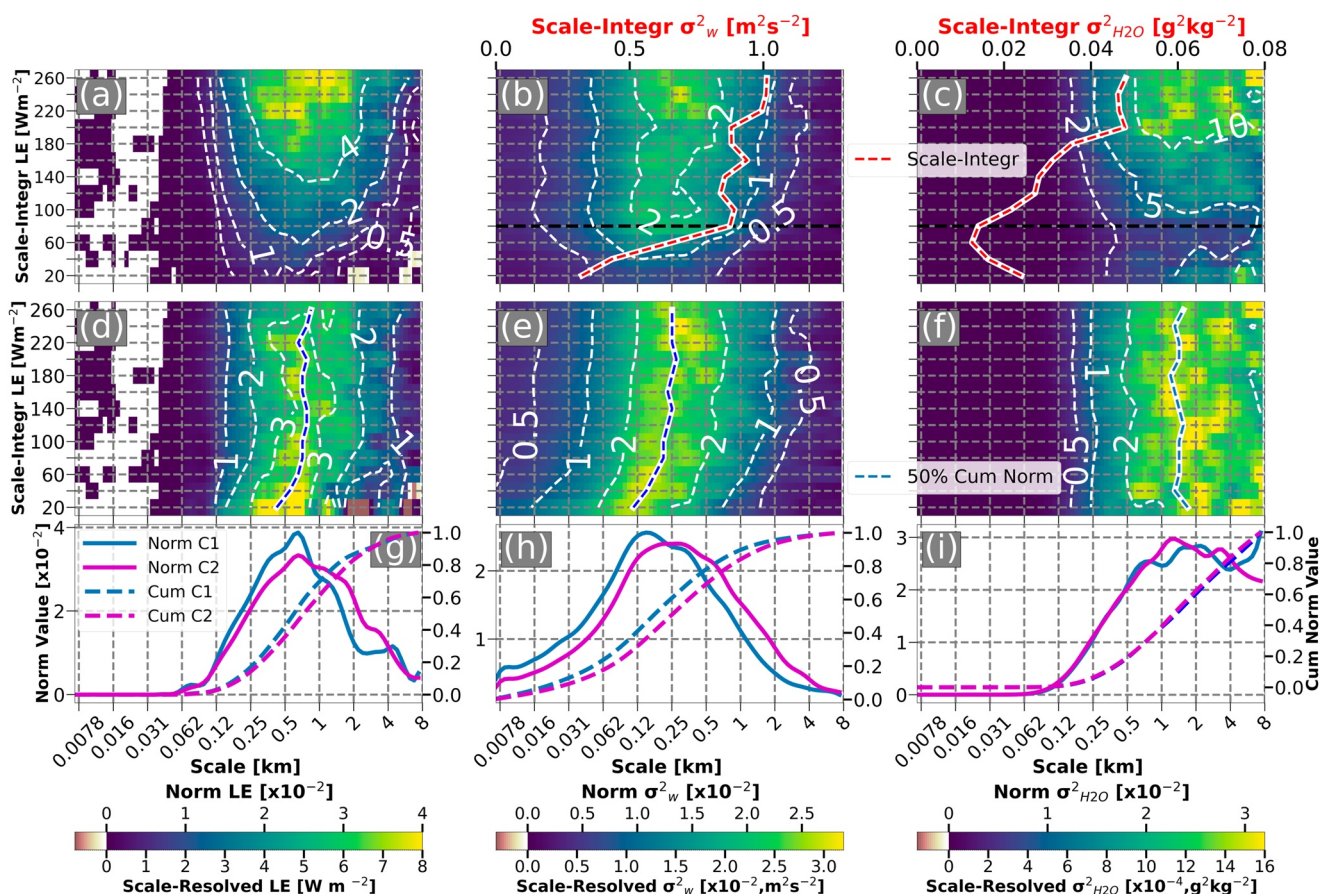


Figure 7. The scale-dependent (a) LE, (b) σ_w^2 , and (c) σ_{H2O}^2 , and normalized scale-dependent (d) LE, (e) σ_w^2 , and (f) σ_{H2O}^2 distributions as a function of leg-integrated total LE from 20 to 260 $W\ m^{-2}$; The distributions of normalized scale-dependent and cumulative (g) LE, (h) σ_w^2 , and (i) σ_{H2O}^2 for low-LE (from 20 to 80 $W\ m^{-2}$) legs, referred to as C1, and for high-LE (from 100 to 260 $W\ m^{-2}$) legs, referred to as C2. The normalized scale-dependent value is the scale-dependent value divided by the integrated value. The white dashed contours in panels (a–f) represent the normalized values (see color bar below). The red-dashed lines in panels (a–c) represent the leg-averaged scale-integrated values; the blue dashed lines in panels (d–f) represent the scale of the median LE scale (50% cumulative values).

260 $W\ m^{-2}$ (Figure 7d). In the meantime, the normalized scale-resolved σ_w^2 with values greater than 1% range shifting from 16–800 m to 50 m to 2 km, and the normalized scale-resolved σ_{H2O}^2 with values greater than 0.5% ranges from 150 m to 8 km as the total LE increases. The 50% cumulative normalized scale-resolved LE is located in scale from 420 to 700 m as total LE increases from 20 to 80 $W\ m^{-2}$ and then maintains its scales at ~700 m from 100 to 260 $W\ m^{-2}$. The 50% cumulative normalized scale-resolved σ_w^2 also has an increasing trend in the scale from 120 to 250 m as total LE from 20 to 120 $W\ m^{-2}$ and then maintains its location around 250 m as total LE increases to 260 $W\ m^{-2}$. The scale of 50% cumulative normalized scale-resolved σ_{H2O}^2 is located around 1.2–1.7 km without an increasing trend.

Based on normalized and cumulative values, the scale-resolved LEs are divided into two categories. The first category (C1) contains low total LE 100 m AGL flight legs (between 20 and 80 $W\ m^{-2}$), while the second category (C2) contains high total LE values (between 100 and 260 $W\ m^{-2}$), as shown in Figures 7g–7i. The normalized scale-resolved LE in C1 is larger than that in C2 in scales ranging from 250 to 800 m, while normalized scale-resolved LE in C2 is larger than that in C1 in scales ranging from 800 m to 4 km. The same pattern is observed in the distribution of normalized scale-resolved σ_w^2 , but with the separation scale at 250 m (Figures 7g and 7h). The distribution of normalized scale-resolved LE and σ_w^2 are different for the two categories. However, the normalized scale-resolved σ_{H2O}^2 has the same values from 8 to 800 m in C1 and C2. The cumulative normalized values show the percentage of resolved scales in LE, σ_w^2 , and σ_{H2O}^2 .

Operational numerical weather prediction (NWP) systems can use scale-resolved normalized and cumulative values to guide sub-grid scale parameterization. The highest-resolution non-hydrostatic NWP systems aimed at

real-time forecasting approach a horizontal grid spacing Δx of around 1 km. For example, the National Severe Storms Laboratory Warn-on-Forecast System (WoFS) has been run in nested CONUS subdomains at $\Delta x = 1$ km (WoFS-1 km) during episodes of anticipated severe weather (Kerr et al., 2023; Y. Wang et al., 2022), while the Application of Research to Operations at Mesoscale model runs at $\Delta x = 1.2$ km, and the Consortium for Small-scale Modeling (COSMO) model runs at $\Delta x = 1.1$ km in parts of Europe (e.g., Benjamin et al., 2019; Dowell et al., 2022). In general, the effective model resolution is coarser than the Nyquist (maximum unresolvable) horizontal wavelength $L_{Nyq} = 2\Delta x$. Following the conventional assumption that modeled horizontal wavelength exceeding $\sim 6-7\Delta x = \sim 3 L_{Nyq}$ is needed to adequately resolve a wavelike phenomenon (Benjamin et al., 2019; Skamarock, 2004), the smallest resolvable horizontal wavelength at $\Delta x = 1$ km grid model is 6 km (see also Chapter 11 in Lackmann 2011). The spectral distribution in Figure 7 indicates that the unresolvable normalized percentages are 99% in LE, 99% in σ_w^2 , and 96% in σ_{H2O}^2 for the highest resolvable resolution of 6 km in the highest-resolution storm-scale NWP systems currently in operation. The scales of 50% cumulative normalized values indicate LE and σ_w^2 are dominated more by the forcings on smaller scales, compared to that in σ_{H2O}^2 . Thus, the unresolvable scale-dependent values driven by scales smaller than NWP resolution must be individually parameterized in LE, σ_w^2 , and σ_{H2O}^2 in the NWP systems.

3.3.2. Temporal Dependency

To investigate the temporal variability of scale-resolved LE, σ_w^2 , and σ_{H2O}^2 , the LE is composited on 20 flight legs from morning to afternoon in flight IOPs of July, August, and September (Figures 8a–8c). Even though the first flight took off at different times and the sunrise and sunset times varied in RFs of IOPs from July to September (Table 1), the same legs from all four RFs in the morning and in the afternoon in each IOP are averaged. The distribution of scale-resolved LE with values greater than 2 W m^{-2} becomes narrow from 120 m–4 km in July to 250 m–2 km in September, showing flight-leg dependent temporal variability in each month (Figure 8a). Similarly, the distribution of scale-resolved σ_{H2O}^2 with values greater than $1 \times 10^{-4} \text{ g kg}^{-2}$ becomes narrow from 120 m–8 km in July to 250 m–4 km in September (Figure 8c). However, the distribution of scale-resolved σ_w^2 differs from that in scale-resolved LE and σ_{H2O}^2 , with values greater than $0.5 \times 10^{-2} \text{ m}^2 \text{ s}^{-2}$ observed in 32 m–4 km in August, but changes to 10 m–3 km in July and September (Figure 8b). Similarly, the monthly mean total LE and total σ_{H2O}^2 decrease from July to September, but the monthly mean total σ_w^2 has the smallest value in August (Table 2). The monthly standard deviations of total LE are 20–35 W m^{-2} indicating strong temporal variation in all monthly IOPs.

To investigate the relative scale distributions of LE, σ_w^2 , and σ_{H2O}^2 , the normalized scale-resolved LE, σ_w^2 , and σ_{H2O}^2 are calculated based on legs in IOPs. The range of normalized scale-resolved LEs is from 120 m to 4 km for values greater than 1% of the cumulative normalized LE (Figure 8d). The scale variation is shown as the scale of 50% of cumulative normalized scale-resolved LE (blue dashed lines in Figures 8d–8f). The monthly mean scale of 50% of cumulative normalized scale-resolved LE ranges from 580 m in July to 670 m in September. In the meantime, the normalized scale-resolved σ_w^2 distribution with values greater than 1% is mainly located between 32 m and 2 km (Figure 8e). The monthly mean scale of 50% of cumulative normalized scale-resolved σ_w^2 has the largest value of 260 m in August, and smaller values in July (180 m) and September (140 m). The normalized scale-resolved σ_{H2O}^2 with a value greater than 1% ranges between 200 m and 8 km in all IOPs (Figure 8f). The monthly mean scale of 50% of cumulative normalized scale-resolved σ_{H2O}^2 ranges from 1.06 to 1.43 km. Even though temporal variations exist in flight legs and in IOPs, the normalized scale-resolved distributions and mean scale of 50% of the cumulative normalized scale-resolved value change small in LE, σ_w^2 , and σ_{H2O}^2 , respectively. The primary contribution to scale-resolved LE should be in the overlap scales between σ_w^2 (32 m–2 km) and σ_{H2O}^2 (200 m–8 km) ranging between 200 m and 2 km, which coincides with the primary scale-resolved LE distribution with values greater than 2% ranging from 200 m to 2 km. Despite the different scale distribution between σ_w^2 and σ_{H2O}^2 , the primary scale contribution between 200 m and 2 km from σ_w^2 and σ_{H2O}^2 to LE indicates large eddies in the PBL primary sources of vertical moisture transport.

3.4. The Contributions of Turbulent, Large, and Mesoscale Eddies on LE

3.4.1. Total LE Dependency

To better understand the scale-dependent impacts of w' and r_v' to LE, the scales from 8 m to 8 km are classified into three ranges. Previous studies (e.g., Mauder et al., 2007; Paleri et al., 2022) used a 2 km threshold to separate

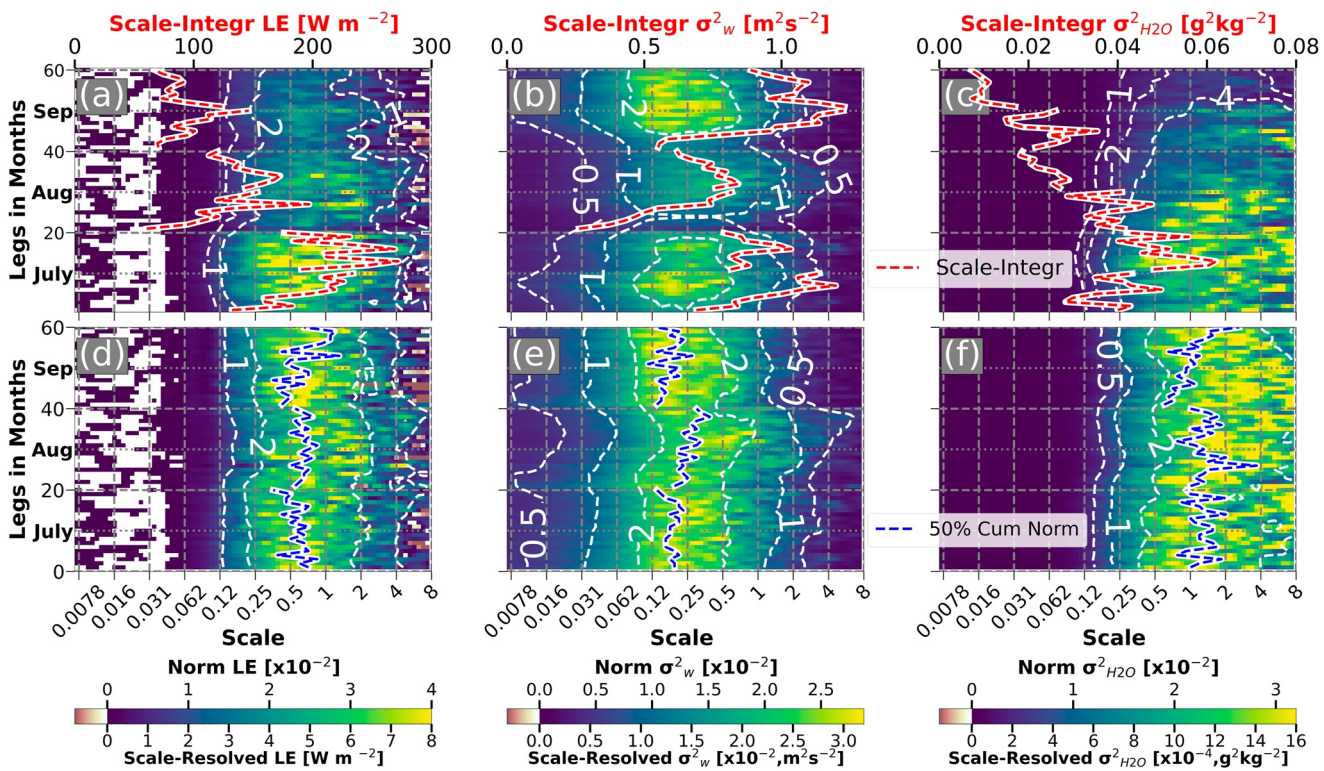


Figure 8. As in Figure 7 (a–f), but as a function of leg numbers (y-axis) averaged monthly Intensive Observation Periods in July, August, and September.

the scales between the small turbulent PBL scale and the larger mesoscale to isolate the mesoscale contributions to the total LE. Our analysis of scale-resolved σ_w^2 shows that the primary scale-resolved σ_w^2 occurs within a wavelength of 2 km (Figures 7e and 8e), which aligns with the PBL depth. Orlanski (1975) used a threshold scale of 200 m to differentiate between turbulence (micro γ scale < 20 m through 20 m \leq micro β scale < 200 m) and organized eddies (200 m \leq micro α scale < 2 km through 2 km \leq meso γ scale < 20 km). Our analysis of scale-resolved σ_w^2 and $\sigma_{\text{H}_2\text{O}}^2$ shows that the 200 m marks the end of σ_w^2 scale contributing to total σ_w^2 and the beginning of the $\sigma_{\text{H}_2\text{O}}^2$ scale contributing to total LE. Thus, the scales are divided into three ranges: 8–200 m (“turbulent” scale in PBL), 200 m–2 km (“large-eddy” scale in PBL), and 2–8 km (“mesoscale”) to explore their contributions to σ_w^2 , $\sigma_{\text{H}_2\text{O}}^2$, and LE under different total LE values and IOP legs. Note that both the turbulent and large-eddy scales fall in the inertial subrange for isotropic turbulence in the surface layer (Stull, 1988).

The scale-resolved LE in the three scale ranges increases as the total LE increases from 20 to 260 W m^{-2} , but the percentage contributions to total LE among the three scale ranges only slightly change (Figure 9a). The large-eddy scale contributes to the highest percentage of total LE, ranging from 69% to 75% (the orange dashed line in Figure 9a), followed by the mesoscale contribution (the blue dashed line), and the turbulent-scale contribution (the red dashed line) is the smallest. The majority of the σ_w^2 is found in turbulent and large eddy scales, accounting for over 90% of the total σ_w^2 . The mesoscale σ_w^2 contribution is less than 10% of the total σ_w^2 . As the total LE increases from 20 to 100 W m^{-2} , the turbulent σ_w^2 decreases \sim 20%, while the σ_w^2 in the large-eddy scale increases \sim 20%. The σ_w^2 variations indicate the turbulent eddies transform to large eddies as total LE varies from 20 to 100 W m^{-2} . On the other hand, the $\sigma_{\text{H}_2\text{O}}^2$ is mainly found in the large-eddy scale and mesoscale, accounting for over 96% of total $\sigma_{\text{H}_2\text{O}}^2$, while the turbulent scale $\sigma_{\text{H}_2\text{O}}^2$ is only 3%–4% of total $\sigma_{\text{H}_2\text{O}}^2$, which could be biased by the temporal response of the water vapor sensor.

To examine the scale contribution from the covariance of w' and r_v' to the LE, $\text{cov}_{(w', H_2O)}$ in the three scale ranges is calculated based on Equation 9 (dotted lines in Figure 9a). The mean difference between $\text{cov}_{(w', H_2O)}$ and LE

Table 2

The Monthly Leg-Averaged Mean, the Standard Deviation, and the Monthly Mean Scale of 50% Cumulative Values in LE, σ_w^2 , and $\sigma_{\text{H}_2\text{O}}^2$

Variable	July	Aug	Sep	
LE	Mean \pm Std (W m^{-2})	207 ± 35	133 ± 30	91 ± 20
	Mean of 50% scales (km)	0.58	0.65	0.67
σ_w^2	Mean \pm Std ($\times 10^{-2}$, $\text{m}^2 \text{s}^{-2}$)	92 ± 13	65 ± 16	97 ± 20
	Mean of 50% scales (km)	0.18	0.26	0.14
$\sigma_{\text{H}_2\text{O}}^2$	Mean \pm Std ($\times 10^{-3}$, $\text{g}^2 \text{kg}^{-2}$)	45 ± 9	31 ± 9	16 ± 8
	Mean of 50% scales (km)	1.29	1.43	1.06

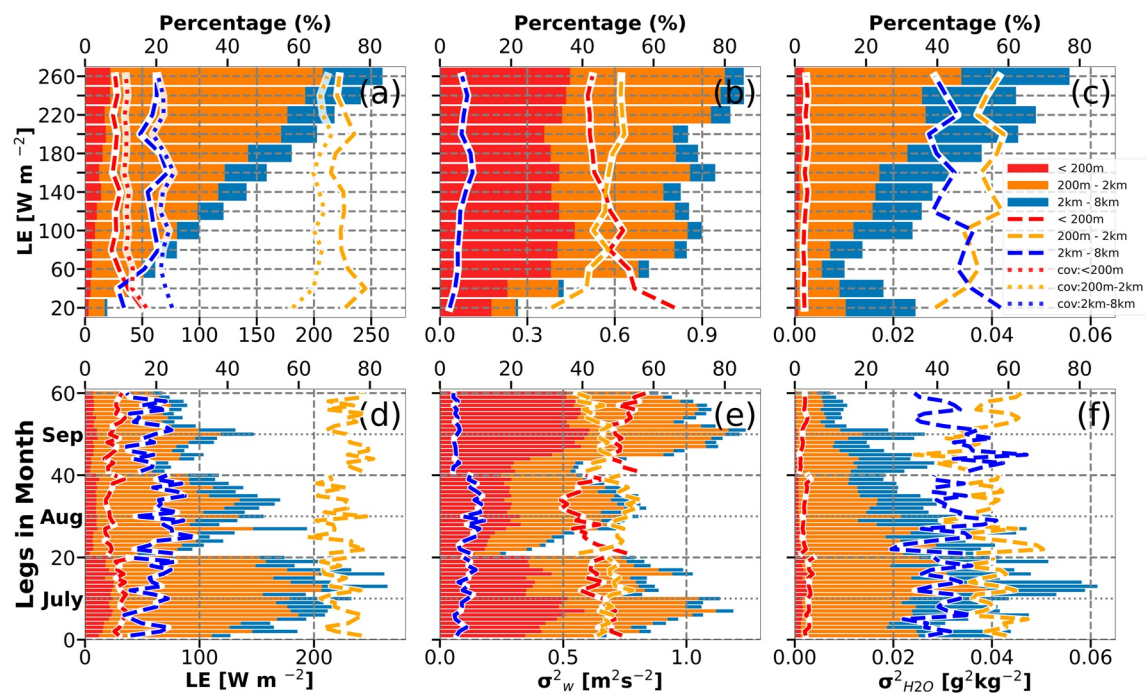


Figure 9. The partitions of turbulent scale (red), large eddy scale (orange), and mesoscale (blue) contributions based on leg-integrated LE in LE (a, d), σ_w^2 (b, e), and σ_{H2O}^2 (c, f) sorted with LE from 20 to 260 W m⁻² (a–c) and leg time (d–f). The red-, orange-, and blue-dashed lines represent the leg-averaged scale-integrated contributions (expressed as percentages) from turbulent scale, large-eddy scale, and mesoscale respectively. The dotted lines in panel (a) are the corresponding $\text{cov}_{(w, H2O)}$ averages in the three scale ranges.

is less than 10% of the total LE. The largest mean difference between $\text{cov}_{(w, H2O)}$ and LE is observed in the large-eddy scale, accounting for 7%. The mean difference in turbulent scale and mesoscale is 3% and 4% of total LE, respectively. The most significant difference is observed in the total LE between 20 and 60 W m⁻², particularly the difference of 15% in the mesoscale as the total LE ranges from 20 to 40 W m⁻². Overall, the analysis of $\text{cov}_{(w, H2O)}$ revealed similar results to the directly calculated LE, with the majority of LE found in the large-eddy scale, followed by the mesoscale, and the smallest percentage of the total LE found in the turbulent scale.

3.4.2. Temporal Dependency

The contributions in different scale ranges to monthly IOP-mean total LEs are similar to the previous analysis, but temporal variations exist in legs and in IOPs (Table 3 and Figure 9d–9f). The temporal variations in IOPs are represented by standard deviations. The temporal variations mainly arise from the first two significant contributing scales, which are the large-eddy and mesoscale in LE (3.8%–4.4%), turbulent and large-eddy scales in σ_w^2 (2.2%–4.7%), as well as large-eddy scale and mesoscale in σ_{H2O}^2 (4.8%–7.8%). However, the least contribution to temporal variation is the turbulent LE (1.2%–1.5%), mesoscale σ_w^2 (0.6%–2.1%), and turbulent σ_{H2O}^2 (0.6%–0.7%).

3.5. Forcing Scales of w' and r_v' : Implications and Additional Evidence

Results above indicated that the scale forcings are different in σ_w^2 and σ_{H2O}^2 to LE. The primary scale forcings are the large-eddy scale and mesoscale in LE, the turbulent scale and large-eddy scale in σ_w^2 , and the large-eddy scale and mesoscale in σ_{H2O}^2 . Couvreux et al. (2005, 2006) investigated r_v variability in the CBL with airborne measurements and LES and also found that the characteristic length scale of r_v is larger than w . Both observations and LES indicate the intrusions of dry free-troposphere air into the growing CBL. These intrusions generally lack negative buoyancy but they may interact

Table 3

The Monthly Leg-Averaged Mean and the Standard Deviation in LE, σ_w^2 , and σ_{H2O}^2 in Three Spatial Ranges (Turbulent Scale, Large-Eddy Scale, and Mesoscale), Expressed as a Percentage of the Total

Variable	July		August		September		
	Mean	Std	Mean	Std	Mean	Std	
LE	Turb (%)	10	1.3	7	1.2	8	1.5
	Large-eddy (%)	71	3.8	70	4.4	75	3.9
	Meso (%)	19	4.3	23	4.4	17	4.0
σ_w^2	Turb (%)	45	3.0	41	4.7	52	2.9
	Large-eddy (%)	48	2.2	50	3.7	44	2.8
	Meso (%)	7	1.6	9	2.1	4	0.6
σ_{H2O}^2	Turb (%)	4	0.6	3	0.6	2	0.7
	Large-eddy (%)	55	4.8	54	6.9	52	7.8
	Meso (%)	41	5.0	43	7.1	46	8.3

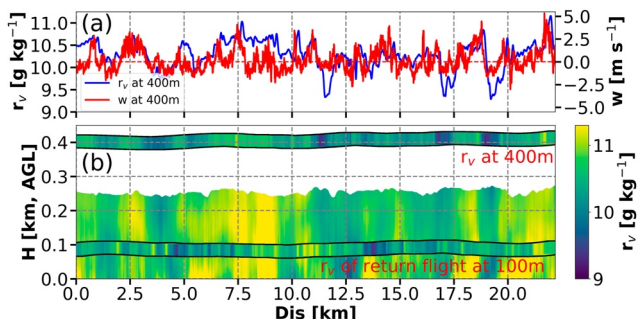


Figure 10. (a) Flight-level r_v (blue line) and w (red line) for RF03 leg 2 at 400 m Above Ground Level (AGL). (b) Flight-level in situ r_v and CRL 2D profile of r_v . The colored return flight at 100 m AGL is the r_v along the flight leg in Figure 2, where the flight track is the same as this flight, but at a different height.

with large-eddy circulations that transport the drier free-troposphere into the lower CBL, and occasionally even close to the surface. Moreover, Couvreux et al. (2005, 2006) found that large amounts of dry air that are quickly incorporated into the CBL prevent full homogenization by turbulent mixing. Near the heated land surface, these dry air intrusions may become negatively buoyant. The entrainment and/or horizontal advection could cause phase shifting in large-eddy w and r_v , leading to LE decreasing (Gao et al., 2017). In our study, the flight tracks at 400 m AGL with CRL measurements provide 2D vertical profiles of r_v to investigate the vertical r_v distribution and transport process (Figure 10). For instance, the 400 m AGL flight in situ data measured downward transport (negative flight-level w) of relatively drier air ($\sim 9.2 \text{ g kg}^{-1}$) at the distance of 11.5, 17, and 18.5 km (Figure 10a). The CRL samples these three drier air parcels and shows that they penetrated toward the 100 m AGL (Figure 10b). The horizontal scales of dry and moist air parcels (PBL large eddies) sampled by CRL are a few kilometers, which is consistent with the return flight-level $\sigma_{\text{H}_2\text{O}}^2$ scaling from 200 m to 8 km at 100 m AGL in Figure 2i, indicating large-eddy and mesoscale forcings in r_v .

Since the time difference between the 400 and 100 m flight legs is 5–10 min, and the chosen RFs that are closest perpendicular to the prevailing wind, the r_v at 100 m AGL between CRL and flight level data do not correspond very well by perpendicular advection. However, r_v shows a shift of dry air ($\sim 9 \text{ g kg}^{-1}$) from 12.5 km for the CRL measurement to 13.5 km for the airborne in situ measurement at around 100 m AGL. Although lacking 2D w' profiles from the airborne measurements, variability in w' at smaller scales than r_v' is observed at 400 m AGL (Figure 10a). Moreover, w' at the 100 m return flight shows small-scale variability between 16 m and 1.5 km (Figure 2h) indicating the dominant turbulent and large-eddy scale forcings.

4. Discussions and Conclusions

The leg-averaged and scale-resolved LE show seasonal variations from July to September. The wavelet technique applied to high-frequency airborne data allows us to analyze atmospheric flux contributions from the turbulent scale to the mesoscale above heterogeneous terrain during the CHEESEHEAD19 field campaign. The leg-averaged LE in July was 250 W m^{-2} in a single 3-hr RF, decreasing to 80 W m^{-2} in September. The scale-resolved LE in RFs mainly distributes between 62 m and 8 km with scale-resolved temporal variability. However, the general diurnal patterns of leg-averaged LE did not occur for all IOP days, thus highlighting the significant roles of PBL circulation and mesoscale advection in controlling local LEs regardless of radiation. These temporal variations are related to the combination of differences in surface types, wind conditions, and net radiation as the aircraft samples in space and time and require rectification and footprint-identification approaches for any mapping of LE using airborne data (Metzger et al., 2013; Y. Sun et al., 2023).

The contributions of LE, σ_w^2 , and $\sigma_{\text{H}_2\text{O}}^2$ from three scale categories are quantified. The three main conclusions are as follows:

- The dominant scale is rather short for w (32 m–2 km), longer for r_v (200 m–8 km), and intermediate for LE (120 m–4 km), which depends on the covariance of w and r_v . The scale differences could also be measured with the scales of 50% of cumulative normalized scale-resolved LE ($\sim 600 \text{ m}$), σ_w^2 ($\sim 200 \text{ m}$), and $\sigma_{\text{H}_2\text{O}}^2$ ($\sim 1.2 \text{ km}$)
- Most variance in LE, σ_w^2 , and $\sigma_{\text{H}_2\text{O}}^2$ is found in the large-eddy scale (0.2–2.0 km), with σ_w^2 containing substantial variability also in the turbulent scale (8–200 m) and $\sigma_{\text{H}_2\text{O}}^2$ in the mesoscale (2–8 km). The large-scale eddies contribute 70% of total LE and about 50% of the total σ_w^2 and the total $\sigma_{\text{H}_2\text{O}}^2$. Thus, the large eddies are the primary sources of vertical moisture transport across the PBL. The surface forcing and boundary layer circulations could drive the scale up to the PBL height ($\sim 2 \text{ km}$).
- The distribution of scale-resolved $\sigma_{\text{H}_2\text{O}}^2$ is different than the LE and σ_w^2 distributions, mainly in the mesoscale. The mesoscale contributes $\sim 43\%$ of total water vapor variations, which drives the $\sim 20\%$ mesoscale contributions of total LE. The entrainment of dry air from the free troposphere, PBL circulation, and mesoscale horizontal advection could lead to observed significant mesoscale water vapor variations.

The large-eddy scale in PBL is not fully resolved by the current finest-resolution operational regional non-hydrostatic NWP systems with horizontal grid spacings near 1 km (Dowell et al., 2022). With a 1 km model

grid, the minimum resolvable size of a feature is about 6 km (e.g., Chapter 11 in Lackmann 2011). The unresolved cumulative normalized percentages within scales less than 6 km are 99% in LE, 99% in σ_w^2 , and 94%–96% in σ_{H2O}^2 . These high percentages of unresolvable scale-dependent values driven by scales smaller than the NWP resolution explain the continued needs for PBL parameterizations in NWP models for LE, σ_w^2 , and σ_{H2O}^2 , respectively. The results emphasize that scale-dependent PBL parameterizations are necessary to capture the complex nature of PBL processes.

Clearly, this analysis complements published LE variations on scales, which primarily present scale-dependent LE analysis and lack detailed scale-dependent vertical velocity and water vapor contributing information to LE. The different dominant scale distributions among LE, σ_w^2 , and σ_{H2O}^2 need to be carefully considered in PBL parameterizations. Although the results presented here may be limited to the daytime PBL in the summer of northern Wisconsin, the methodology presented here could be applied to future measurements in other locations under different surface heterogeneities. The PBL will need to be parameterized in NWP models in the foreseeable future. Thus, results from other surface and dynamical conditions could be critical to provide data to improve scale-dependent PBL parameterizations.

Future studies should further explore the height-dependent scale-resolved LE and the impacts of w and r_v on LE. The dominant scales of LE, w , and r_v are height-dependent, as evident from airborne measurements and LES simulations (Couvreux et al., 2005). The w and r_v in PBL are determined by not only surface evapotranspiration, but entrainment from the free atmosphere, PBL circulation and depth, and mesoscale advection (Linné et al., 2006). Compared to flight-level in situ data at 100 m AGL, the dominant scale at a higher level could shift to larger scales as the surface influence becomes less, and stronger influenced by PBL circulation, entrainment, and mesoscale advection. Future analysis of CHEESEHEAD19 measurements at 400 m cloud be used to explore height-dependent scale-decencies although it is not possible to provide continuous height-dependency. By applying the wavelet technique to airborne in situ data collected at multiple flight levels, or, better, by combining full profiles of airborne Raman lidar r_v data with Doppler lidar w measurements could effectively characterize the height-dependent scale-resolved LE. Further studies should also compare and synergize atmospheric fluxes between the airborne measurements and model simulations to improve the parameterization of the PBL fluxes (Hu et al., 2023).

Data Availability Statement

The UWKA in situ data and surface-based flux tower data are available on the EOL CHEESEHEAD19 website (https://www.eol.ucar.edu/field_projects/cheesehead). The land cover classification of NLCD 2019 can be found on the Multi-Resolution Land Characteristics Consortium (MRLC) website (<https://www.mrlc.gov/data/nlcd-2019-land-cover-conus>).

References

- Attié, J.-L., & Durand, P. (2003). Conditional wavelet technique applied to aircraft data measured in the thermal internal boundary layer during sea-breeze events. *Boundary-Layer Meteorology*, 106(3), 359–382. <https://doi.org/10.1023/a:1021262406408>
- Aubinet, M., Vesala, T., & Papale, D. (2012). Eddy covariance: A practical guide to measurement and data analysis. <https://doi.org/10.1007/978-94-007-2351-1>
- Avissar, R., & Schmidt, T. (1998). An evaluation of the scale at which ground-surface heat flux patchiness affects the convective boundary layer using large-eddy simulations. *Journal of the Atmospheric Sciences*, 55(16), 2666–2689. [https://doi.org/10.1175/1520-0469\(1998\)055<2666:AEots>2.0.Co;2](https://doi.org/10.1175/1520-0469(1998)055<2666:AEots>2.0.Co;2)
- Bange, J., Beyrich, F., & Engelbart, D. A. M. (2002). Airborne measurements of turbulent fluxes during LITFASS-98: Comparison with ground measurements and remote sensing in a case study. *Theoretical and Applied Climatology*, 73(1), 35–51. <https://doi.org/10.1007/s00704-002-0692-6>
- Benjamin, S. G., Brown, J. M., Brunet, G., Lynch, P., Saito, K., & Schlatter, T. W. (2019). 100 Years of progress in forecasting and NWP applications. *Meteorological Monographs*, 59, 13.11–13.67. <https://doi.org/10.1175/amsmonographs-d-18-0020.1>
- Berger, B. W., Davis, K. J., Yi, C., Bakwin, P. S., & Zhao, C. L. (2001). Long-term carbon dioxide fluxes from a very tall tower in a northern forest: Flux measurement methodology. *Journal of Atmospheric and Oceanic Technology*, 18(4), 529–542. [https://doi.org/10.1175/1520-0426\(2001\)018<0529:Ltdff>2.0.Co;2](https://doi.org/10.1175/1520-0426(2001)018<0529:Ltdff>2.0.Co;2)
- Betts, A. K. (1982). Saturation point analysis of moist convective overturning. *Journal of the Atmospheric Sciences*, 39(7), 1484–1505. [https://doi.org/10.1175/1520-0469\(1982\)039<1484:Spaomc>2.0.Co;2](https://doi.org/10.1175/1520-0469(1982)039<1484:Spaomc>2.0.Co;2)
- Beyrich, F., Herzog, H. J., & Neisser, J. (2002). The LITFASS project of DWD and the LITFASS-98 experiment: The project strategy and the experimental setup. *Theoretical and Applied Climatology*, 73(1–2), 3–18. <https://doi.org/10.1007/s00704-002-0690-8>
- Beyrich, F., & Mengelkamp, H.-T. (2006). Evaporation over a heterogeneous land surface: EVA_GRIPS and the LITFASS-2003 Experiment—An overview. *Boundary-Layer Meteorology*, 121(1), 5–32. <https://doi.org/10.1007/s10546-006-9079-z>

Acknowledgments

This study was funded and supported by the National Science Foundation (NSF) Grants AGS-1917693 and AGS-1917701, by the Department of Energy (DOE) Atmospheric System Research (ASR) Grant SC0020171, and by the National Aeronautics and Space Administration (NASA) 80NSSC20K0663, with additional support for scientific airborne data collection activities from the University of Wyoming King Air team. ADR acknowledges support from the NSF AGS-2313772. The CHEESEHEAD19 field campaign was supported by NSF Grant AGS-1822420. US-PFa observations were supported by a subaward to ARD from the DOE Ameriflux Network Management Project. The CHEESEHEAD19 data are provided by NSF-funded NCAR/EOL via the respective projects' Field Catalogs. The present study benefited from the hard work of the many additional CHEESEHEAD19 participants to collect the data that helped enable this study. This manuscript benefits from the excellent and detailed comments offered by the formal reviewers.

- Bou-Zeid, E., Anderson, W., Katul, G. G., & Mahrt, L. (2020). The persistent challenge of surface heterogeneity in boundary-layer meteorology: A review. *Boundary-Layer Meteorology*, 177(2–3), 227–245. <https://doi.org/10.1007/s10546-020-00551-8>
- Butterbach-Bahl, K., Kögel-Knabner, I., & Han, X. (2011). Steppe ecosystems and climate and land-use changes—Vulnerability, feedbacks and possibilities for adaptation. *Plant and Soil*, 340(1–2), 1–6. <https://doi.org/10.1007/s11104-010-0651-4>
- Butterworth, B. J., Desai, A. R., Townsend, P. A., Petty, G. W., Andresen, C. G., Bertram, T. H., et al. (2021). Connecting land-atmosphere interactions to surface heterogeneity in CHEESEHEAD19. *Bulletin of the American Meteorological Society*, 102(2), E421–E445. <https://doi.org/10.1175/bams-d-19-0346.1>
- Charuchittipan, D., Babel, W., Mauder, M., Leps, J. P., & Foken, T. (2014). Extension of the averaging time in eddy-covariance measurements and its effect on the energy balance closure. *Boundary-Layer Meteorology*, 152(3), 303–327. <https://doi.org/10.1007/s10546-014-9922-6>
- Couvreux, F., Guichard, F., Masson, V., & Redelsperger, J. L. (2006). Negative water vapour skewness and dry tongues in the convective boundary layer: Observations and large-eddy simulation budget analysis. *Boundary-Layer Meteorology*, 123(2), 269–294. <https://doi.org/10.1007/s10546-006-9140-y>
- Couvreux, F., Guichard, F., Redelsperger, J. L., Kiemle, C., Masson, V., Lafore, J. P., & Flamant, C. (2005). Water-vapour variability within a convective boundary-layer assessed by large-eddy simulations and IHOP_2002 observations. *Quarterly Journal of the Royal Meteorological Society*, 131(611), 2665–2693. <https://doi.org/10.1256/qj.04.167>
- Davis, K. J., Bakwin, P. S., Yi, C., Berger, B. W., Zhao, C., Teclaw, R. M., & Isebrands, J. G. (2003). The annual cycles of CO₂ and H₂O exchange over a northern mixed forest as observed from a very tall tower. *Global Change Biology*, 9(9), 1278–1293. <https://doi.org/10.1046/j.1365-2486.2003.00672.x>
- Desai, A. R. (2023). AmeriFlux BASE US-PFa park falls/WLEF [Dataset]. AmeriFlux AMP, Ver. 24–5. <https://doi.org/10.17190/AMF/1246090>
- Desai, A. R., Bolstad, P. V., Cook, B. D., Davis, K. J., & Carey, E. V. (2005). Comparing net ecosystem exchange of carbon dioxide between an old-growth and mature forest in the upper Midwest, USA. *Agricultural and Forest Meteorology*, 128(1–2), 33–55. <https://doi.org/10.1016/j.agrformet.2004.09.005>
- Desai, A. R., Murphy, B. A., Wiesner, S., Thom, J., Butterworth, B. J., Koupaei-Abyazani, N., et al. (2022). Drivers of decadal carbon fluxes across temperate ecosystems. *Journal of Geophysical Research: Biogeosciences*, 127(12), e2022JG007014. <https://doi.org/10.1029/2022JG007014>
- Desai, A. R., Paleri, S., Mineau, J., Kadum, H., Wanner, L., Mauder, M., et al. (2022). Scaling land-atmosphere interactions: Special or fundamental? *Journal of Geophysical Research: Biogeosciences*, 127(10), e2022JG007097. <https://doi.org/10.1029/2022JG007097>
- Desjardins, R. L., MacPherson, J. I., Mahrt, L., Schuepp, P., Pattey, E., Neumann, H., et al. (1997). Scaling up flux measurements for the boreal forest using aircraft-tower combinations. *Journal of Geophysical Research*, 102(D24), 29125–29133. <https://doi.org/10.1029/97jd00278>
- Desjardins, R. L., MacPherson, J. I., Neumann, H., Den Hartog, G., & Schuepp, P. H. (1995). Flux estimates of latent and sensible heat, carbon dioxide, and ozone using an aircraft-tower combination. *Atmospheric Environment*, 29(21), 3147–3158. [https://doi.org/10.1016/1352-2310\(95\)00007-1](https://doi.org/10.1016/1352-2310(95)00007-1)
- Dewitz, J., & U.S. Geological Survey. (2021). National land cover Database (NLCD) 2019 products [Dataset]. U.S. Geological Survey data release, Ver. 2.0. <https://doi.org/10.5066/P9KZCM54>
- Dowell, D. C., Alexander, C. R., James, E. P., Weygandt, S. S., Benjamin, S. G., Manikin, G. S., et al. (2022). The high-resolution rapid refresh (HRRR): An hourly updating convection-allowing forecast model. Part I: Motivation and system description. *Weather and Forecasting*, 37(8), 1371–1395. <https://doi.org/10.1175/Waf-D-21-0151.1>
- Eder, F., Schmidt, M., Damian, T., Träumer, K., & Mauder, M. (2015). Mesoscale eddies affect near-surface turbulent exchange: Evidence from lidar and tower measurements. *Journal of Applied Meteorology and Climatology*, 54(1), 189–206. <https://doi.org/10.1175/jamc-d-14-0140.1>
- Farge, M. (1992). Wavelet transforms and their applications to turbulence. *Annual Review of Fluid Mechanics*, 24(1), 395–457. <https://doi.org/10.1146/annurev.fl.24.010192.002143>
- Finnigan, J. J., Clement, R., Malhi, Y., Leuning, R., & Cleugh, H. A. (2003). A re-evaluation of long-term flux measurement techniques Part I: Averaging and coordinate rotation. *Boundary-Layer Meteorology*, 107(1), 1–48. <https://doi.org/10.1023/A:1021554900225>
- Fischer, L., Craig, G. C., & Kiemle, C. (2013). Horizontal structure function and vertical correlation analysis of mesoscale water vapor variability observed by airborne lidar. *Journal of Geophysical Research: Atmospheres*, 118(14), 7579–7590. <https://doi.org/10.1002/jgrd.50588>
- Foken, T., Aubinet, M., Finnigan, J. J., Leclerc, M. Y., Mauder, M., & Paw U. K. T. (2011). Results of A panel discussion about the energy balance closure correction for trace gases. *Bulletin of the American Meteorological Society*, 92(4), ES13–ES18. <https://doi.org/10.1175/2011bams3130.1>
- Foken, T., Göockede, M., Mauder, M., Mahrt, L., Amiro, B., & Munger, W. (2004). Post-field data quality control. In *Handbook of micrometeorology* (Vol. 119, pp. 181–208). Kluwer Academic Publishers.
- Foken, T., & Wichura, B. (1996). Tools for quality assessment of surface-based flux measurements. *Agricultural and Forest Meteorology*, 78(1–2), 83–105. [https://doi.org/10.1016/0168-1923\(95\)02248-1](https://doi.org/10.1016/0168-1923(95)02248-1)
- French, J., Oolman, L., & Plummer, D. (2021). University of Wyoming king air (UWKA) high rate flight level data [Dataset]. UCAR/NCAR - Earth Observing Laboratory. Version 1.0. <https://doi.org/10.26023/5B70-4VP5-XY0V>
- Gao, Z., Liu, H., Katul, G., & Foken, T. (2017). Non-closure of the surface energy balance explained by phase difference between vertical velocity and scalars of large atmospheric eddies. *Environmental Research Letters*, 12(3), 034025. <https://doi.org/10.1088/1748-9326/aa625b>
- Gao, Z., Liu, H. P., Russell, E. S., Huang, J. P., Foken, T., & Oncley, S. P. (2016). Large eddies modulating flux convergence and divergence in a disturbed unstable atmospheric surface layer. *Journal of Geophysical Research: Atmospheres*, 121(4), 1475–1492. <https://doi.org/10.1002/2015jd024529>
- Garratt, J. (1994). Review: The atmospheric boundary layer. *Earth-Science Reviews*, 37(1–2), 89–134. [https://doi.org/10.1016/0016-8252\(94\)90026-4](https://doi.org/10.1016/0016-8252(94)90026-4)
- Haimov, S., & Rodi, A. (2013). Fixed-antenna pointing-angle calibration of airborne Doppler cloud radar. *Journal of Atmospheric and Oceanic Technology*, 30(10), 2320–2335. <https://doi.org/10.1175/Jtech-D-12-0026.1>
- Halldin, S., Gryning, S. E., Gottschalk, L., Jochum, A., Lundin, L. C., & Van de Griend, A. A. (1999). Energy, water and carbon exchange in a boreal forest landscape — NOPEX experiences. *Agricultural and Forest Meteorology*, 98–99, 5–29. [https://doi.org/10.1016/s0168-1923\(99\)00148-3](https://doi.org/10.1016/s0168-1923(99)00148-3)
- Helbig, M., Gerken, T., Beamesderfer, E. R., Baldocchi, D. D., Banerjee, T., Biraud, S. C., et al. (2021). Integrating continuous atmospheric boundary layer and tower-based flux measurements to advance understanding of land-atmosphere interactions. *Agricultural and Forest Meteorology*, 307, 108509. <https://doi.org/10.1016/j.agrformet.2021.108509>
- Hill, T. C., Williams, M., & Moncrieff, J. B. (2008). Modeling feedbacks between a boreal forest and the planetary boundary layer. *Journal of Geophysical Research*, 113(D15), D15122. <https://doi.org/10.1029/2007jd009412>
- Hill, T. C., Williams, M., Woodward, F. I., & Moncrieff, J. B. (2011). Constraining ecosystem processes from tower fluxes and atmospheric profiles. *Ecological Applications*, 21(5), 1474–1489. <https://doi.org/10.1890/09-0840.1>
- Hu, X. M., Gourdji, S. M., Davis, K. J., Wang, Q., Zhang, Y., Xue, M., et al. (2021). Implementation of improved parameterization of terrestrial flux in WRF-VPRM improves the simulation of nighttime CO₂ peaks and a daytime CO₂ band ahead of a cold front. *Journal of Geophysical Research: Atmospheres*, 126(10), e2020JD034362. <https://doi.org/10.1029/2020JD034362>

- Hu, X. M., Huang, Y., Xue, M., Martin, E., Hong, Y., Chen, M., et al. (2023). Effects of lower troposphere vertical mixing on simulated clouds and precipitation over the Amazon during the wet season. *Journal of Geophysical Research: Atmospheres*, 128(12), e2023JD038553. <https://doi.org/10.1029/2023jd038553>
- Hudgins, L. H. (1992). Wavelet analysis of atmospheric turbulence.
- Kerr, C. A., Matilla, B. C., Wang, Y., Stratman, D. R., Jones, T. A., & Yussouf, N. (2023). Results from a Pseudo-real-time next-generation 1-km warn-on-forecast system prototype. *Weather and Forecasting*, 38(2), 307–319. <https://doi.org/10.1175/waf-d-22-0080.1>
- Kiemle, C., Brewer, W. A., Ehret, G., Hardsty, R. M., Fix, A., Senff, C., et al. (2007). Latent heat flux profiles from collocated airborne water vapor and wind lidars during IHOP_2002. *Journal of Atmospheric and Oceanic Technology*, 24(4), 627–639. <https://doi.org/10.1175/jtech1997.1>
- LeMone, M. A., Angevine, W. M., Bretherton, C. S., Chen, F., Dudhia, J., Fedorovich, E., et al. (2019). 100 Years of progress in boundary layer meteorology. *Meteorological Monographs*, 59, 9.1–9.85. <https://doi.org/10.1175/amsmonographs-d-18-0013.1>
- Lin, G., Geerts, B., Wang, Z. E., Grasnick, C., Jing, X. Q., & Yang, J. (2019). Interactions between a nocturnal MCS and the stable boundary layer as observed by an airborne compact Raman lidar during PECAN. *Monthly Weather Review*, 147(9), 3169–3189. <https://doi.org/10.1175/Mwr-D-18-0388.1>
- Lin, G., Grasnick, C., Geerts, B., Wang, Z. E., & Deng, M. (2021). Convection initiation and bore formation following the collision of mesoscale boundaries over a developing stable boundary layer: A case study from PECAN. *Monthly Weather Review*, 149(7), 2351–2367. <https://doi.org/10.1175/Mwr-D-20-0282.1>
- Lin, G., Wang, Z., Ziegler, C., Hu, X.-M., Xue, M., Geerts, B., & Chu, Y. (2023). A comparison of convective storm inflow moisture variability between the great plains and the southeastern United States using multiplatform field campaign observations. *Journal of Atmospheric and Oceanic Technology*, 40(5), 539–556. <https://doi.org/10.1175/jtech-d-22-0037.1>
- Linné, H., Hennemuth, B., Bösenberg, J., & Ertel, K. (2006). Water vapour flux profiles in the convective boundary layer. *Theoretical and Applied Climatology*, 87(1–4), 201–211. <https://doi.org/10.1007/s00704-005-0191-7>
- Liu, B., Wang, Z., Cai, Y., Wechsler, P., Kuestner, W., Burkhardt, M., & Welch, W. (2014). Compact airborne Raman lidar for profiling aerosol, water vapor and clouds. *Optics Express*, 22(17), 20613–20621. <https://doi.org/10.1364/OE.22.020613>
- Mahrt, L. (1998). Flux sampling errors for aircraft and towers. *Journal of Atmospheric and Oceanic Technology*, 15(2), 416–429. [https://doi.org/10.1175/1520-0426\(1998\)015<0416:Fsefa>2.0.Co;2](https://doi.org/10.1175/1520-0426(1998)015<0416:Fsefa>2.0.Co;2)
- Mahrt, L. (2000). Surface heterogeneity and vertical structure of the boundary layer. *Boundary-Layer Meteorology*, 96(1–2), 33–62. <https://doi.org/10.1023/a:1002482332477>
- Mahrt, L. (2010). Computing turbulent fluxes near the surface: Needed improvements. *Agricultural and Forest Meteorology*, 150(4), 501–509. <https://doi.org/10.1016/j.agrformet.2010.01.015>
- Margairaz, F., Pardyjak, E. R., & Calaf, M. (2020). Surface thermal heterogeneities and the atmospheric boundary layer: The relevance of dispersive fluxes. *Boundary-Layer Meteorology*, 175(3), 369–395. <https://doi.org/10.1007/s10546-020-00509-w>
- Mauder, M., Desjardins, R. L., & MacPherson, I. (2007). Scale analysis of airborne flux measurements over heterogeneous terrain in a boreal ecosystem. *Journal of Geophysical Research*, 112(D13), D13112. <https://doi.org/10.1029/2006jd008133>
- Mauder, M., Foken, T., & Cuxart, J. (2020). Surface-energy-balance closure over land: A review. *Boundary-Layer Meteorology*, 177(2–3), 395–426. <https://doi.org/10.1007/s10546-020-00529-6>
- Mauder, M., Jegede, O. O., Okogbue, E. C., Wimmer, F., & Foken, T. (2006). Surface energy balance measurements at a tropical site in West Africa during the transition from dry to wet season. *Theoretical and Applied Climatology*, 89(3–4), 171–183. <https://doi.org/10.1007/s00704-006-0252-6>
- Metzger, S., Durden, D., Paleri, S., Sühring, M., Butterworth, B. J., Florian, C., et al. (2021). Novel approach to observing system simulation experiments improves information gain of surface-atmosphere field measurements. *Atmospheric Measurement Techniques*, 14(11), 6929–6954. <https://doi.org/10.5194/amt-14-6929-2021>
- Metzger, S., Junkermann, W., Mauder, M., Butterbach-Bahl, K., Trancón y Widemann, B., Neidl, F., et al. (2013). Spatially explicit regionalization of airborne flux measurements using environmental response functions. *Biogeosciences*, 10(4), 2193–2217. <https://doi.org/10.5194/bg-10-2193-2013>
- Oncley, S. (2021). NCAR/EOL 5 minute ISFS surface flux data, tilt corrected, geographic coordinate winds [Dataset]. UCAR/NCAR - Earth Observing Laboratory, Version 2.1. <https://doi.org/10.26023/43MF-NP8N-3Q0V>
- Orlanski, I. (1975). A rational subdivision of scales for atmospheric processes. *Bulletin of the American Meteorological Society*, 56(5), 527–534. <https://doi.org/10.1175/1520-0477-56.5.527>
- Paleri, S., Desai, A. R., Metzger, S., Durden, D., Butterworth, B. J., Mauder, M., et al. (2022). Space-scale resolved surface fluxes across a heterogeneous, mid-latitude forested landscape. *Journal of Geophysical Research: Atmospheres*, 127(23), e2022JD037138. <https://doi.org/10.1029/2022jd037138>
- Pielke, R. A., Avissar, R., Sr., Raupach, M., Dolman, A. J., Zeng, X., & Denning, A. S. (2003). Interactions between the atmosphere and terrestrial ecosystems: Influence on weather and climate. *Global Change Biology*, 9(5), 461–475. <https://doi.org/10.1046/j.1365-2486.1998.t01-1-00176.x>
- Pielke, R. A., Lee, T. J., Copeland, J. H., Eastman, J. L., Ziegler, C. L., & Finley, C. A. (1997). Use of USGS-provided data to improve weather and climate simulations. *Ecological Applications*, 7(1), 3–21. [https://doi.org/10.1890/1051-0761\(1997\)007\[0003:Uoupd\]2.0.Co;2](https://doi.org/10.1890/1051-0761(1997)007[0003:Uoupd]2.0.Co;2)
- Platis, A., Moene, A. F., Villagrasa, D. M., Beyrich, F., Tupman, D., & Bange, J. (2017). Observations of the temperature and humidity structure parameter over heterogeneous terrain by airborne measurements during the LITFASS-2003 campaign. *Boundary-Layer Meteorology*, 165(3), 447–473. <https://doi.org/10.1007/s10546-017-0290-x>
- Pressel, K. G., Collins, W. D., & Desai, A. R. (2014). The spatial scale dependence of water vapor variability inferred from observations from a very tall tower. *Journal of Geophysical Research: Atmospheres*, 119(16), 9822–9837. <https://doi.org/10.1002/2013jd021141>
- Raupach, M. R., & Finnigan, J. J. (1995). Scale issues in boundary-layer meteorology - Surface-energy balances in heterogeneous terrain. *Hydrological Processes*, 9(5–6), 589–612. <https://doi.org/10.1002/hyp.3360090509>
- Sellers, P., Hall, F., Ranson, K. J., Margolis, H., Kelly, B., Baldocchi, D., et al. (1995). The boreal ecosystem-atmosphere study (BOREAS): An overview and early results from the 1994 field year. *Bulletin of the American Meteorological Society*, 76(9), 1549–1577. [https://doi.org/10.1175/1520-0477\(1995\)076<1549:Tbesao>2.0.Co;2](https://doi.org/10.1175/1520-0477(1995)076<1549:Tbesao>2.0.Co;2)
- Sherwood, S. C., Roca, R., Weckwerth, T. M., & Andronova, N. G. (2010). Tropospheric water vapor, convection, and climate. *Reviews of Geophysics*, 48(2), RG2001. <https://doi.org/10.1029/2009rg000301>
- Skamarock, W. C. (2004). Evaluating mesoscale NWP models using kinetic energy spectra. *Monthly Weather Review*, 132(12), 3019–3032. <https://doi.org/10.1175/mwr2830.1>

- Steinfeld, G., Letzel, M. O., Raasch, S., Kanda, M., & Inagaki, A. (2007). Spatial representativeness of single tower measurements and the imbalance problem with eddy-covariance fluxes: Results of a large-eddy simulation study. *Boundary-Layer Meteorology*, 123(1), 77–98. <https://doi.org/10.1007/s10546-006-9133-x>
- Stevens, B., & Bony, S. (2013). Water in the atmosphere. *Physics Today*, 66(6), 29–34. <https://doi.org/10.1063/pt.3.2009>
- Strunin, M. A., & Hiyama, T. (2005). Spectral structure of small-scale turbulent and mesoscale fluxes in the atmospheric boundary layer over a thermally inhomogeneous land surface. *Boundary-Layer Meteorology*, 117(3), 479–510. <https://doi.org/10.1007/s10546-005-2188-2>
- Stull, R. B. (1988). *An introduction to boundary layer meteorology* (Vol. 13). Springer Science & Business Media.
- Stull, R. B. (2015). *Practical meteorology—an algebra-based Survey of atmospheric science*. University of British Columbia.
- Sun, X.-M., Zhu, Z.-L., Wen, X.-F., Yuan, G.-F., & Yu, G.-R. (2006). The impact of averaging period on eddy fluxes observed at ChinaFLUX sites. *Agricultural and Forest Meteorology*, 137(3–4), 188–193. <https://doi.org/10.1016/j.agrformet.2006.02.012>
- Sun, Y., Jia, L., Chen, Q., Lin, X., Sude, B., Quan, Z., & Hutjes, R. W. A. (2023). Construction of a spatially gridded heat flux map based on airborne flux Measurements using remote sensing and machine learning methods. *Agricultural and Forest Meteorology*, 334, 109424. <https://doi.org/10.1016/j.agrformet.2023.109424>
- Thomas, C., & Foken, T. (2004). Detection of long-term coherent exchange over spruce forest using wavelet analysis. *Theoretical and Applied Climatology*, 80(2–4), 91–104. <https://doi.org/10.1007/s00704-004-0093-0>
- Torrence, C., & Compo, G. P. (1998). A practical guide to wavelet analysis. *Bulletin of the American Meteorological Society*, 79(1), 61–78. [https://doi.org/10.1175/1520-0477\(1998\)079<0061:Apgtwa>2.0.Co;2](https://doi.org/10.1175/1520-0477(1998)079<0061:Apgtwa>2.0.Co;2)
- Vadrevu, K. P., & Choi, Y. (2011). Wavelet analysis of airborne CO₂ measurements and related meteorological parameters over heterogeneous landscapes. *Atmospheric Research*, 102(1–2), 77–90. <https://doi.org/10.1016/j.atmosres.2011.06.008>
- Wang, H., Feingold, G., Wood, R., & Kazil, J. (2010). Modelling microphysical and meteorological controls on precipitation and cloud cellular structures in Southeast Pacific stratocumulus. *Atmospheric Chemistry and Physics*, 10(13), 6347–6362. <https://doi.org/10.5194/acp-10-6347-2010>
- Wang, Y., Yussouf, N., Kerr, C. A., Stratman, D. R., & Matilla, B. C. (2022). An experimental 1-km warn-on-forecast system for hazardous weather events. *Monthly Weather Review*, 150(11), 3081–3102. <https://doi.org/10.1175/mwr-d-22-0094.1>
- Wang, Z. (2020). Airborne Compact Raman lidar (CRL) water vapor and temperature profiles [Dataset]. UCAR/NCAR - Earth Observing Laboratory. Version 2.0. <https://doi.org/10.26023/JYNH-KCZE-910F>
- Wang, Z., Wechsler, P., Kuestner, W., French, J., Rodi, A., Glover, B., et al. (2009). Wyoming cloud lidar: Instrument description and applications. *Optics Express*, 17(16), 13576–13587. <https://doi.org/10.1364/OE.17.013576>
- Wolf, B., Chwala, C., Fersch, B., Garvelmann, J., Junkermann, W., Zeeman, M. J., et al. (2017). The SCALEX campaign: Scale-crossing land surface and boundary layer processes in the TERENO-preAlpine observatory. *Bulletin of the American Meteorological Society*, 98(6), 1217–1234. <https://doi.org/10.1175/bams-d-15-00277.1>
- Wu, D., Wang, Z., Wechsler, P., Mahon, N., Deng, M., Glover, B., et al. (2016). Airborne compact rotational Raman lidar for temperature measurement. *Optics Express*, 24(18), A1210–A1223. <https://doi.org/10.1364/OE.24.0A1210>